



Corrosion and passivation of AlCrFe₂Ni₂Mo_x high-entropy alloys in sulphuric acid

Jakub Czerski ^{a,*}, Marzena Mitoraj-Królikowska ^a, Elżbieta Godlewska ^a, Annica Wetzel ^b, Julia Witt ^b, Ozlem Ozcan ^b, Mateusz Marzec ^c, Marcin Goły ^d

^a AGH University of Krakow, Faculty of Materials Science and Ceramics, Al. Mickiewicza 30, Krakow, Poland

^b Bundesanstalt für Materialforschung und -prüfung (BAM), D-12205 Berlin, Germany

^c AGH University of Krakow, Academic Centre for Materials and Nanotechnology, al. Mickiewicza 30, Krakow, Poland

^d AGH University of Krakow, Faculty of Metals Engineering and Industrial Computer Science, al. Mickiewicza 30, Krakow, Poland



ARTICLE INFO

Keywords:

- A. Alloy
- A. Sulphuric acid
- B. AFM
- B. EIS
- C. Acid corrosion
- C. Passive films

ABSTRACT

Corrosion behaviour of AlCrFe₂Ni₂Mo_x ($x = 0.0, 0.1, 0.15, 0.3$ and 0.6) high-entropy alloys was investigated in a $0.1\text{ M H}_2\text{SO}_4$ solution. Passive films formed upon anodic polarisation, built of Al-based inner layer and (Cr, Fe, Mo)-based outer layer, had good protective properties. In particular, they prevented corrosion of the (Al, Ni)-rich BCC-B2 phase, which was observed under open-circuit conditions. Moderate amounts of Mo, up to $x = 0.3$, positively affected the passivation ability of AlCrFe₂Ni₂. Significant changes in microstructure and phase composition of the alloy at higher Mo concentrations ($x = 0.6$) resulted in deterioration of its corrosion resistance.

1. Introduction

The Al-Co-Cr-Fe-Ni alloys, composed of finely distributed FCC and BCC phases in the eutectic or spinodally decomposed microstructures [1–6], are the most extensively investigated among high-entropy alloys (HEAs). Recently, however, there has been growing interest in cost-effective Co-free alloys with very similar phase compositions and properties [7–9]. Although there are numerous data on the microstructure and mechanical properties of the AlCoCrFeNi alloys in the literature [10–13], much less is known about their corrosion resistance [14–18], and even less about the chemical properties of these alloys without Co [16–20]. The electrolyte most often used in these studies was NaCl. Only a few papers describe the corrosion properties of Al-Co-Cr-Fe-Ni alloys in H_2SO_4 solutions [21–27], and not even one is dedicated to the quaternary Al-Cr-Fe-Ni alloys.

Molybdenum is one of the additives used to improve hardness, yield strength, or corrosion resistance of various alloys. Although its beneficial effect on the passivation of stainless steels is well documented [28–33], its influence on the HEAs is still unclear. To date, not a single article has been dedicated to the impact of Mo on the corrosion properties of HEAs from Al-Co-Cr-Fe-Ni system, and only two focused on the cobalt-free system, Al-Cr-Fe-Ni [17–34] (both performed in sodium

chloride solutions). Most of the previous investigations dealt with the CoCrFeNiMo_x compositions [35–42].

In [35], Hu et al. interpreted the corrosion behaviour of CoCrFeNiMo_x HEAs in H_2SO_4 solution in terms of competition between the beneficial Cr_2O_3 enrichment of the passive film and detrimental phase transformation, FCC $\rightarrow \sigma$, which induced selective (galvanic) corrosion and hindered the development of uniform passive film. The best effects, found for CoCrFeNiMo_{0.6}, were attributed to the maximum enrichment of the passive film in Cr_2O_3 , although the alloy had unfavourable hypoeutectic microstructure with coexisting FCC and σ phases. Similar observations were presented by Shang et al. [36], while Dai et al. [38] suggested that the protective ability of passive films is mainly based on their composition and, more specifically, on the Cr/Mo concentration ratio, due to the synergistic effect of these elements. It follows from previous corrosion studies of HEAs (mainly CoCrFeNiMo_x alloys) that small additions of Mo can be beneficial for the stability of passive films, but higher amounts usually lead to segregation of Mo and Cr into intermetallic phases, such as the σ phase, and galvanic corrosion between the (Cr, Mo)-depleted matrix and the (Cr, Mo)-rich precipitates [43]. The σ phase, typically occurring in alloys containing Fe, Cr and Mo, such as stainless steels, is highly undesirable due to depletion of neighbouring grains in Mo and Cr, and deterioration of their corrosion

* Corresponding author.

E-mail address: jczerski@agh.edu.pl (J. Czerski).

resistance [44,45]. Niu et al. [41] indicated brittleness and intense localised corrosion of CoCrFeNiMo_x alloys with higher concentrations of Mo, which were attributed to σ and μ phases, while Dai et al. reported their worse ability to form passive films in both NaCl [37] and H₂SO₄ [38].

Among the Co-free medium entropy alloys, the most investigated is AlCrFe₂Ni₂ with a nanoscale duplex microstructure spontaneously formed by spinodal decomposition [7–12], which appeared particularly interesting for additive manufacturing. After the first successful results obtained by laser powder-bed fusion (LPBF) [46,47] or laser metal deposition (LMD) [48,49], the manufacturing processes were further improved [50]. It follows from our previous investigations that small additions of Mo in AlCrFe₂Ni₂ alloys are beneficial for the mechanical properties and corrosion resistance [18–29]. Some of the AlCrFe₂Ni₂Mo_x alloys had ultimate tensile strength (UTS) of 2000 MPa and ductility over 20% [51], and might be considered as cost-effective replacements of super-duplex stainless steels with UTS of 1600 MPa, provided their corrosion resistance is sufficient. So far, AlCrFe₂Ni₂Mo_x alloys ($x = 0.00 - 0.15$) were tested in 3.5 wt% NaCl and showed corrosion rates of less 10⁻³ mm/yr [17]. In the current study, alloys with Mo concentrations extending up to 9.6 at% are tested in sulphuric acid (0.1 M H₂SO₄), with the objective of gaining insight into the role of Mo in the formation of passive films. Topography, as well as microstructure and composition of alloys surface are analysed at various stages of electrochemical measurements. The experimental techniques used comprise cyclic potentiodynamic polarisation (CPP), electrochemical impedance spectroscopy (EIS) and atomic force microscopy (AFM), as well as X-ray diffraction (XRD), scanning electron microscopy (SEM), energy dispersive X-ray spectrometry (EDS) and X-ray photoelectron spectroscopy (XPS).

2. Experimental procedures

2.1. Samples preparation

Alloys with the compositions given in Table 1, further in the text referred to as Mo_x (Mo₀, Mo_{0.1}, Mo_{0.15}, Mo_{0.3} and Mo_{0.6}), were produced at Access e.V., Aachen, via arc melting of the metallic components (purities above 99.8 wt%) under argon into 300-g buttons. Each button was remelted at least 3 times for homogenisation and suction cast into rods with a diameter of 10 mm, which were cut by wire electrical discharge machining. For electrochemical testing, the samples were embedded in an epoxy resin together with copper wire connections attached to each sample by means of a conductive silver lacquer. Before the measurement, the working electrode was ground with SiC abrasive papers from 400 to 1200 grit and cleaned with isopropanol. Samples intended for SEM and XPS analyses were additionally polished with a 1- μ m diamond suspension.

Table 1

Chemical compositions of investigated AlCrFe₂Ni₂Mo_x alloys determined by EDS (at%).

Alloy	Notation	Al	Cr	Fe	Ni	Mo
AlCrFe ₂ Ni ₂	Mo ₀	16.3 ± 0.0	17.3 ± 0.0	33.8 ± 0.2	32.6 ± 0.2	-
AlCrFe ₂ Ni ₂ Mo _{0.10}	Mo _{0.1}	15.5 ± 0.2	17.2 ± 0.1	33.7 ± 0.0	32.0 ± 0.0	1.7 ± 0.0
AlCrFe ₂ Ni ₂ Mo _{0.15}	Mo _{0.15}	15.2 ± 0.1	17.0 ± 0.1	33.4 ± 0.0	31.9 ± 0.1	2.5 ± 0.0
AlCrFe ₂ Ni ₂ Mo _{0.30}	Mo _{0.3}	14.8 ± 0.2	16.4 ± 0.1	32.4 ± 0.1	31.5 ± 0.1	4.8 ± 0.1
AlCrFe ₂ Ni ₂ Mo _{0.60}	Mo _{0.6}	14.1 ± 0.2	15.6 ± 0.1	30.7 ± 0.2	30.0 ± 0.2	9.6 ± 0.1

2.2. Materials characterization

The structure of AlCrFe₂Ni₂Mo_x alloys was analysed by XRD using a Siemens D500 diffractometer with Cu-K α radiation in Bragg-Brentano geometry in the 2 θ range of 30–100° with a step size of 0.04° and scan step time of 10 s. The microstructures of alloys before electrochemical measurements were examined by means of a high-resolution scanning electron microscope Merlin Gemini II, ZEISS, equipped with a field-emission gun and Quantax 800 microanalysis system, Bruker, while those after the tests - by a Nova NanoSEM 200 FEI SEM equipped with an EDS for chemical analysis.

2.3. Electrochemical experiments and solution analysis

The electrochemical measurements were performed at room temperature in a three-electrode cell, with an alloy sample as working electrode, a saturated calomel electrode (SCE) as reference electrode, graphite rods as auxiliary electrodes and 0.1 M H₂SO₄ as electrolyte. An SP-150 potentiostat controlled by BioLogic EC-lab V11.25 software was used for CPP tests, while an AUTOLAB PGSTAT 302 N potentiostat driven by Nova 2.1.4 software for 2-h polarisation and EIS. The electrochemical measurements were preceded by a 2-h monitoring of an open-circuit potential (OCP). CPP was carried out according to ASTM G61-86, at a scan rate of 10 mV/min. The scan started at the potential value of −0.3 V vs. OCP and was reversed upon reaching current density of 5 mAcm⁻². Finally, it was terminated at the initial OCP. The potentiostatic polarisation measurements were conducted for 2 h at a potential of 0.6 V_{SCE}, followed by EIS measurements, which were conducted in the frequency range from 100 kHz to 10 mHz, in a single-sine excitation mode with 10 points per decade in a logarithmic spacing. Nova 2.1.4 software was used to generate electrical equivalent circuit (EEC) and fit its parameters. All electrochemical measurements were repeated at least three times.

During the CPP measurements of Mo₀ and Mo_{0.3}, the solution next to the working electrode was collected and analysed using a PerkinElmer Optima 7300 DV inductively coupled plasma optical emission spectrometer (ICP-OES) at the Hydrogeochemical Laboratory of the Department of Hydrogeology and Engineering Geology at AGH University of Krakow, according to ISO 11885:2007. Sampling was done in the middle of the passivation range (0.4 V_{SCE}), at scan reversal point (referred to as 5 mA), at the reverse scan termination point (scan end) and after additional 15 h of immersion without polarisation following the scan end (15 h).

2.4. Passive films characterization

The passive films formed on the surface of AlCrFe₂Ni₂Mo_x alloys were investigated by XPS in two states on the cyclic potentiodynamic curve, i.e., at 0.4 V_{SCE} and at the reversal point of the forward scan (5 mA). The measurements were done in a PHI VersaProbeII Scanning XPS system using monochromatic Al K α (1486.6 eV) X-rays focused to a 100 μ m spot and scanned over the area of 400 μ m × 400 μ m. The photo-electron take-off angle was 45° and the pass energy in the analyser was set to 117.50 eV (0.5 eV step) for survey scans and 46.95 eV (0.1 eV step) to obtain high energy resolution spectra for the Al 2p, Cr 2p, Fe 2p, Ni 2p and Mo 3d regions. A dual beam charge compensation with 7 eV Ar⁺ ions and 1 eV electrons was used to maintain constant potential of sample surface regardless of the sample conductivity. Within the experiment geometry the information depth of analysis was about 5 nm. All XPS spectra were charge referenced to the unfunctionalized, saturated carbon (C-C) C 1 s peak at 285.0 eV. The operating pressure in the analytical chamber was less than 3 × 10⁻⁹ mbar. Deconvolution of spectra was carried out using PHI MultiPak software (v.9.9.0.8). Spectrum background was subtracted using the Shirley method.

2.5. In-situ surface characterization

Prior to the in-situ CPP and 2-h polarisation measurements, the Mo_0 , $\text{Mo}_{0.3}$ and $\text{Mo}_{0.6}$ samples, prepared according to the description in Subsection 2.1, were additionally polished with a 50 nm Al_2O_3 suspension. The freshly polished samples were examined by means of AFM under ambient conditions with a NanoWizard 4 (Bruker Nano GmbH, Germany - formerly known as JPK Instruments) operating in the QI-mode. This technique was used to characterize changes in surface topography during the CPP measurements and during a 2-h polarisation at a potential value of 0.4 V_{SCE}. First scans were done on the polished surface in air and immediately after filling the experimental cell with the electrolyte (0.1 M H_2SO_4). The AFM probe was immersed in the electrolyte during the whole CPP measurement. The AFM images of specimen surface in air were not included in this paper, since they practically did not differ from those in the as-immersed state. In the experimental cell used the sample was working electrode, Pt wire counter electrode and Ag/AgCl was reference electrode. During the CPP scan, polarisation was stopped at the characteristic potential values (0.4 V_{SCE} and potential of scan reverse – 5 mA) to monitor changes on the alloy surface. The AFM images were collected employing a silicon cantilever covered with conductive Cr/Pt-coating (Tap300-G: nominal spring constant of 40 Nm⁻¹ (Budget Sensors, NanoAndMore GmbH, Germany)). The JPK Data Processing Suite (version 6.1.88) was used for an offline analysis of sample topography. After the reversal of CPP scan the surface states of specimens were characterized by SEM images and EDS mapping. A Phenom XL Desktop-scanning electron microscope was used, operated at an accelerating voltage of 15 kV.

3. Results

3.1. Phase composition and microstructure

The results of XRD measurements of $\text{AlCrFe}_2\text{Ni}_2\text{Mo}_x$ alloys are collected in Fig. 1. The BCC phases originating from spinodal decomposition have very similar lattice parameters and are presented without distinction between disordered A2 and ordered B2 [9]. The diffractogram of Mo_0 shows reflections corresponding to the FCC-A1 and BCC phases only. Small additions of molybdenum ($\text{Mo}_{0.1}$ and $\text{Mo}_{0.15}$) did not alter the phase composition. The $\text{Mo}_{0.3}$ diffractogram shows almost exclusively reflections corresponding to BCC, while that of $\text{Mo}_{0.6}$ reveals BCC, σ and possibly minor amounts of FCC. The occurrence of a σ phase at elevated concentrations of Mo is typical of HEAs with similar compositions [36], [37], [42], [51], [52].

The microstructures of $\text{AlCrFe}_2\text{Ni}_2\text{Mo}_x$ alloys are presented in Fig. 2. Nanostructured Mo_0 , $\text{Mo}_{0.1}$ and $\text{Mo}_{0.15}$ characterised earlier in [17] and [53] consist of (Fe, Ni)-rich FCC and two BCC phases, (Fe, Cr)-rich BCC-A2 and (Ni, Al)-rich BCC-B2, formed during the spinodal decomposition. In $\text{Mo}_{0.3}$ the BCC phases are predominant constituents, however in the vicinity of grain boundaries there are brighter spots indicating segregation of another phase. It could be noticed that microstructures of the Mo_0 – $\text{Mo}_{0.3}$ alloys and some thermally treated Al-Co-Cr-Fe-Ni alloys [13], [22] are similar. The microstructure of $\text{Mo}_{0.6}$ is less homogeneous. In addition to the finely interspersed BCC phases from spinodal decomposition, there are many larger grains of (Al, Ni)-rich BCC-B2. Such element segregation was previously reported for alloys with similar compositions in [34], [54], [55].

The EDS elemental mappings for $\text{Mo}_{0.3}$ and $\text{Mo}_{0.6}$ are shown in Figs. 3a and 3b, respectively. The map of $\text{Mo}_{0.3}$ (Fig. 3a) includes a grain boundary triple point, with significant enrichment in Mo, but also elevated concentrations of Cr and Fe. The neighbouring areas (darker in the SEM image) correspond to the spinodally decomposed grains. Although not detected by XRD (Fig. 1), small amounts of σ phase can be present in this alloy. Moreover, Al and Ni in general show the highest intensity next to the Mo-rich grain boundaries. In $\text{Mo}_{0.6}$ (Figure 3b) the segregation of elements is much more pronounced. Al and Ni are present

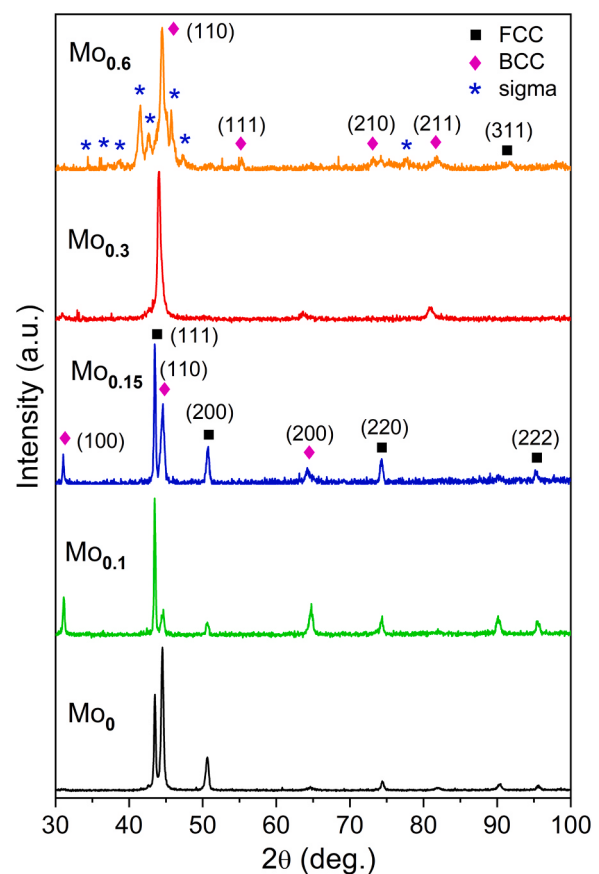


Fig. 1. XRD patterns of $\text{AlCrFe}_2\text{Ni}_2\text{Mo}_x$ alloys. FCC-A1 phase was identified with reference to JCPDS card no. 00-047-1417 for Fe-Ni, BCC-A2 phase - card no. 00-034-0396 for FeCr, BCC-B2 – card no. 00-044-1188 for NiAl, and sigma phase - card no. 98-062-5903 for a tetragonal Cr-Fe structure.

almost exclusively in the round-shaped grains (dark in SEM image), which are distributed all over the surface. Increased amounts of Cr, Fe and Mo can be seen around the biggest BCC-B2 grains, which produce high compositional contrast. Another interesting feature is that Mo segregates to the elongated braid-like bands which are not recognized in elemental maps of other elements and could not be ascribed to any specific phase.

3.2. Cyclic potentiodynamic polarisation tests

The results of cyclic potentiodynamic polarisation are shown in Fig. 4 and Table 2. All materials except $\text{Mo}_{0.6}$ had very similar potential-current characteristics. The corrosion potential (E_{corr}) did not change remarkably with Mo concentration. All alloys showed an active dissolution region, followed by a passive region extending between 0.0 and 0.8 V_{SCE}, until the breakdown potential (E_b) was reached. The current densities were similar and remained almost unchanged for all alloys except $\text{Mo}_{0.6}$. A very narrow negative hysteresis appeared after scan reversal at E_{rev} , suggesting rapid recovery of the protective film [56]. During the reverse scan, current densities were significantly lower than during the forward scan and two anodic to cathodic transitions were observed at about 0.3 and 0.0 V_{SCE}. Passivation current densities, i_{pass} , (measured at 0.4 V_{SCE}) were of only a few μAcm^{-2} . The lowest values of i_{pass} were recorded for Mo_0 and $\text{Mo}_{0.3}$ and these samples were selected for the XPS analyses of the passive films. ICP-OES was used for the analysis of solutions next to the Mo_0 and $\text{Mo}_{0.3}$ working electrodes at several points marked on the CPP curve, defined as 0.4 V, 5 mA, scan end and 15 h in paragraph 2.3 and depicted in Fig. 4.

XPS spectra are presented in Fig. 5 and their quantitative analyses in

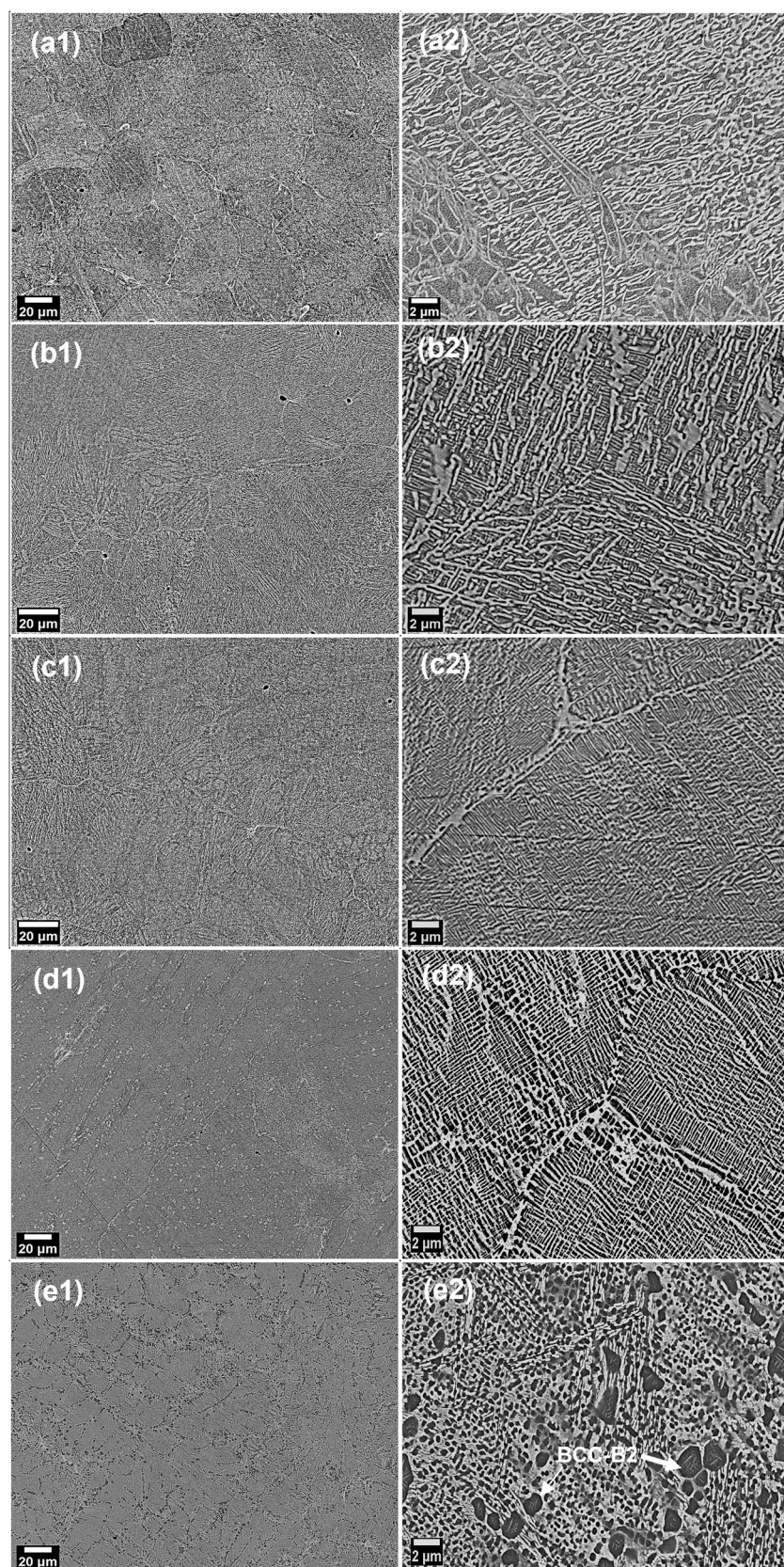


Fig. 2. Back scattered electron (BSE) images of AlCrFe₂Ni₂Mo_x alloys: (a) Mo₀, (b) Mo_{0.1}, (c) Mo_{0.15}, (d) Mo_{0.3} and (e) Mo_{0.6}.

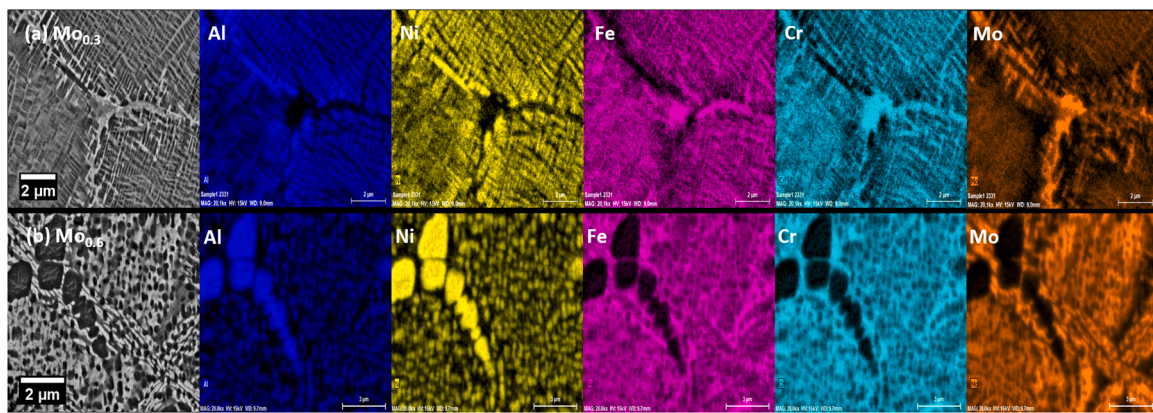


Fig. 3. BSE images and EDS elemental distribution maps for (a) $\text{Mo}_{0.3}$ and (b) $\text{Mo}_{0.6}$.

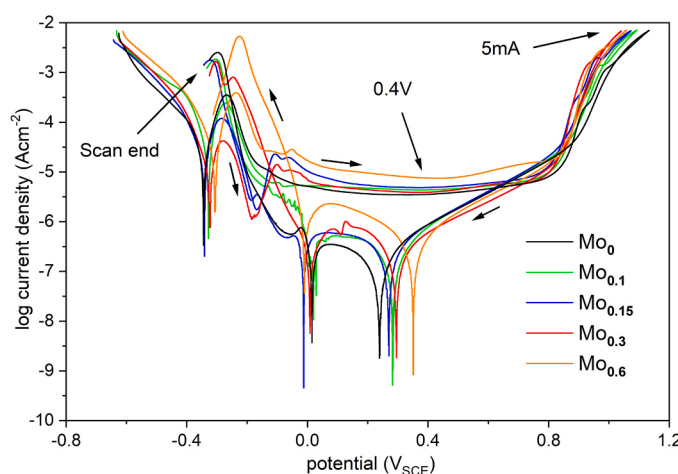


Fig. 4. Representative cyclic potentiodynamic polarisation curves of $\text{AlCrFe}_2\text{-Ni}_2\text{Mo}_X$ alloys in $0.1 \text{ M H}_2\text{SO}_4$. Points 0.4 V, 5 mA and scan end indicate the states selected for subsequent XPS and ICP analyses.

Table 2

Parameters obtained from cyclic potentiodynamic polarisation in $0.1 \text{ M H}_2\text{SO}_4$.

Alloy	E_{corr} [V _{SCE}]	E_b [V _{SCE}]	E_{rev} [V _{SCE}]	i_{pass} [μAcm^{-2}]
Mo_0	-0.35 ± 0.01	0.82 ± 0.01	1.12 ± 0.00	3.3 ± 0.5
$\text{Mo}_{0.1}$	-0.34 ± 0.02	0.80 ± 0.01	1.08 ± 0.01	4.4 ± 0.2
$\text{Mo}_{0.15}$	-0.34 ± 0.02	0.80 ± 0.01	1.07 ± 0.00	4.6 ± 0.9
$\text{Mo}_{0.3}$	-0.32 ± 0.02	0.78 ± 0.02	1.05 ± 0.01	3.4 ± 1.1
$\text{Mo}_{0.6}$	-0.31 ± 0.04	0.80 ± 0.01	1.06 ± 0.04	5.5 ± 1.9

Table 3. Due to ambiguities associated with overlapping of the 2p core level peaks of the transition metals and Auger transition peaks [57], [58], only the oxidation state could be specified, without distinction between the oxide- and hydroxide-type species. The Al 2p spectra were fitted with two lines: the first centred at 72.2 eV, which corresponds to the metallic state of aluminium, and the second broader one at 74.1 eV, which corresponds to the Al^{3+} oxidation state, as in Al_2O_3 or $\text{Al}(\text{OH})_3$ [59], [60]. It should be noted that the derived quantitative data for Al can be less reliable because of the proximity of intensive Ni 3p and Cr 3s lines. The Cr 2p_{3/2} spectra were fitted with two lines: the first centred at 573.7 eV indicating the metallic state of chromium and the second broad one at 576.6 eV - Cr^{3+} oxidation state as in Cr_2O_3 and/or $\text{Cr}(\text{OH})_3$ [61]. The spectra collected in the Fe 2p_{3/2} region are similar for all samples where iron was detected. Each spectrum is fitted with five components, with the first line centred at 706.6 eV, indicating the metallic state of iron, and the second line at 708.3 eV, corresponding to the Fe^{3+}

oxidation state. The three lines within the energy range 710 – 716 eV are due to the multiplet splitting phenomenon and the last line, called shake-up at 715 eV, additionally points out Fe^{3+} [62]. The Ni 2p_{3/2} spectra are similar and show a multiplet splitting structure characteristic of first row transition metal species containing unpaired electrons. From the inspection of the line positions, the first peak centred at 852.4 eV represents the metallic part of Ni and lines in the range from 854 to 864 eV indicate Ni^{2+} oxidation states as in NiO and/or $\text{Ni}(\text{OH})_2$ [63], [64]. The Mo 3d spectra were fitted with three doublet structures ($d_{5/2}$ – $d_{3/2}$ doublet separation equals 3.13 eV) with the first $3d_{5/2}$ line (blue) centred at 227.2 eV corresponding to the metallic state of Mo, the second $3d_{5/2}$ line (green) at 229.8 eV - to Mo^{4+} as in MoO_2 , and the last $3d_{5/2}$ line (magenta) at 232.1 - to Mo^{6+} as in MoO_3 [65].

As indicated in Table 3, at 0.4 V the passive films on Mo_0 and $\text{Mo}_{0.3}$ contained Cr^{3+} , Al^{3+} and Fe^{3+} species in large amounts, and much less those of Ni^{2+} . Mo^{4+} and Mo^{6+} species were also present on the surface of $\text{Mo}_{0.3}$. The main difference between the two alloys at 0.4 V was much lower concentration of $\text{Al}(0)$ and Al^{3+} on the surface of $\text{Mo}_{0.3}$ compared with Mo_0 . The metallic states of all components were detected in the XPS measurements, although only Ni appeared in substantial amounts. As reported by other authors investigating corrosion of stainless steels, the relatively high amounts of $\text{Ni}(0)$ are typical as nickel does not play any significant role in the formation of passive films [66]–[67] and is usually present at increased levels in the region between the oxide film and bulk alloy [68], referred to as ‘a modified alloy layer’ [67]. Therefore, part of the $\text{Ni}(0)$ signal recorded in XPS may originate from the chemically altered substrate, because thickness of the passive film is extremely small. For illustration, on steels [69] or other HEAs [38], [58] it is usually about 3 nm. The low surface concentrations of Ni^{2+} at 0.4 V reflect the fact that other elements are more likely to be oxidized [70], [71], [72]. Molybdenum in the passive film on $\text{Mo}_{0.3}$ was detected as metallic $\text{Mo}(0)$, Mo^{4+} and Mo^{6+} , similarly as reported for other alloys with nearly the same compositions [37], [38]. At 5 mA the surface compositions of both alloys, Mo_0 and $\text{Mo}_{0.3}$, were different: Al^{3+} and Ni^{2+} appeared as the main species, Cr^{3+} at significantly lower amounts and Fe was not detected at all. Although at 0.4 V the amounts of Cr^{3+} on the surface of both alloys were comparable, at 5 mA its amount on $\text{Mo}_{0.3}$ became more than two times higher than on Mo_0 .

The ICP-OES results are given in Table 4. Changes in Al concentration during the potential scan were insignificant for both Mo_0 and $\text{Mo}_{0.3}$. The amounts of other elements in the solution increased, especially after the scan reversal (between 5 mA and scan end). For both alloys, the greatest change in concentrations of ions was observed after additional 15 h of immersion in the solution without polarisation (15 h). The amounts of dissolved ions were much higher at 15 h compared with scan end: in the case of Mo_0 3.6 times for Al, 2.3 times for Cr, 3.6 times for Fe and 5.0 times for Ni, and in the case of $\text{Mo}_{0.3}$ - 3.1 times for Al, 1.3 times for Cr, 1.6 times for Fe and 4.4 times for Ni.

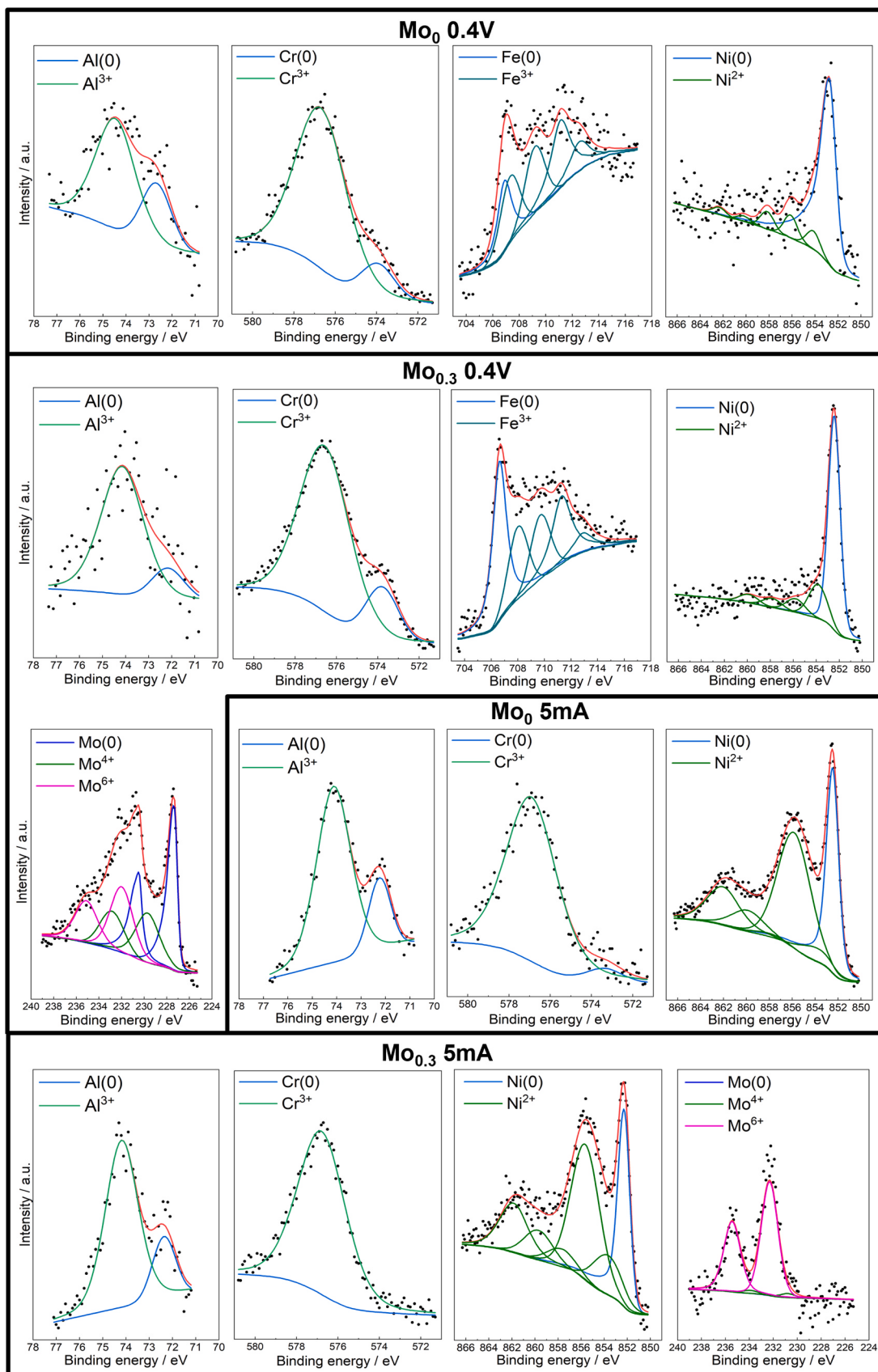


Fig. 5. Deconvoluted XPS spectra of elements detected on the surface of Mo_0 and $\text{Mo}_{0.3}$ samples at $0.4 \text{ V}_{\text{SCE}}$ (0.4 V) and after reaching maximum current density of 5 mA cm^{-2} (5 mA) during CPP, as indicated in Fig. 4. Experimental data are marked with black points, while composite spectra are marked with a red line.

Table 3

Surface compositions of Mo_0 and $\text{Mo}_{0.3}$ at $0.4 \text{ V}_{\text{SCE}}$ and after reaching 5 mA cm^{-2} during CPP (at%).

Energy [eV]	72.2	74.1	573.7	576.6	706.6	708.3	852.4	854	227.2	229.8	232.1
Oxidation state	Al (0)	Al ³⁺	Cr (0)	Cr ³⁺	Fe (0)	Fe ³⁺	Ni (0)	Ni ²⁺	Mo (0)	Mo ⁴⁺	Mo ⁶⁺
Mo_0 , 0.4 V	8.7	22.8	3.9	31.5	3.9	15.0	11.0	3.1	-	-	-
$\text{Mo}_{0.3}$, 0.4 V	2.8	15.6	5.2	28.7	7.3	13.1	11.6	5.2	4.3	2.8	3.4
Mo_0 , 5 mA	10.2	43.0	0.4	7.2	0.0	0.0	12.5	26.8	-	-	-
$\text{Mo}_{0.3}$, 5 mA	7.8	34.4	0.0	16.4	0.0	0.0	9.8	27.7	0.0	0.0	3.9

Table 4

Ion concentrations during CPP measurement of Mo_0 and $\text{Mo}_{0.3}$, determined by ICP-OES.

Sample	Point	Ion content [μM]				
		Al	Cr	Fe	Ni	Mo
Mo_0	0.4 V	3.0	0.6	2.4	2.8	-
	5 mA	3.1	1.0	2.8	2.0	-
	scan end	2.8	2.3	3.5	3.3	-
	15 h	10.6	5.6	12.5	16.5	-
$\text{Mo}_{0.3}$	0.4 V	1.3	< 0.1	0.5	0.4	< 0.1
	5 mA	1.4	< 0.1	0.6	0.5	< 0.1
	scan end	1.7	2.4	4.5	1.6	0.8
	15 h	5.2	3.0	7.0	7.1	1.0

Fig. 6a-d shows the images of surfaces and cross-sections of Mo_0 at the CPP scan end and after additional 15 h of immersion without polarisation. The surface in **Fig. 6a** at the CPP scan end looks blurred but

the initial locations of the FCC phase are easy to recognize. After 15 h of immersion (**Fig. 6b**), the FCC phase is distinctly visible. The average surface composition at the CPP scan end (inset in **Fig. 6a**) shows enrichment in Al and Ni. On the contrary, after 15 h of immersion the surface is depleted in these elements (inset in **Fig. 6b**). From the cross-section in **Fig. 6c** it follows, that the spinodal decomposition area underwent the biggest changes during polarisation. The uncorroded and corroded areas are marked with points 1 and 2, respectively, and their compositions are given in the inset. The composition in point 1 corresponds to the starting material, whereas in point 2 it is depleted in Cr and Fe. The cross-section in **Fig. 6d** shows that the FCC phase is still present near the surface, while the BCC phases from the spinodally decomposed area are leached out.

3.3. In-situ surface characterization

The in-situ AFM imaging in combination with SEM and EDS was

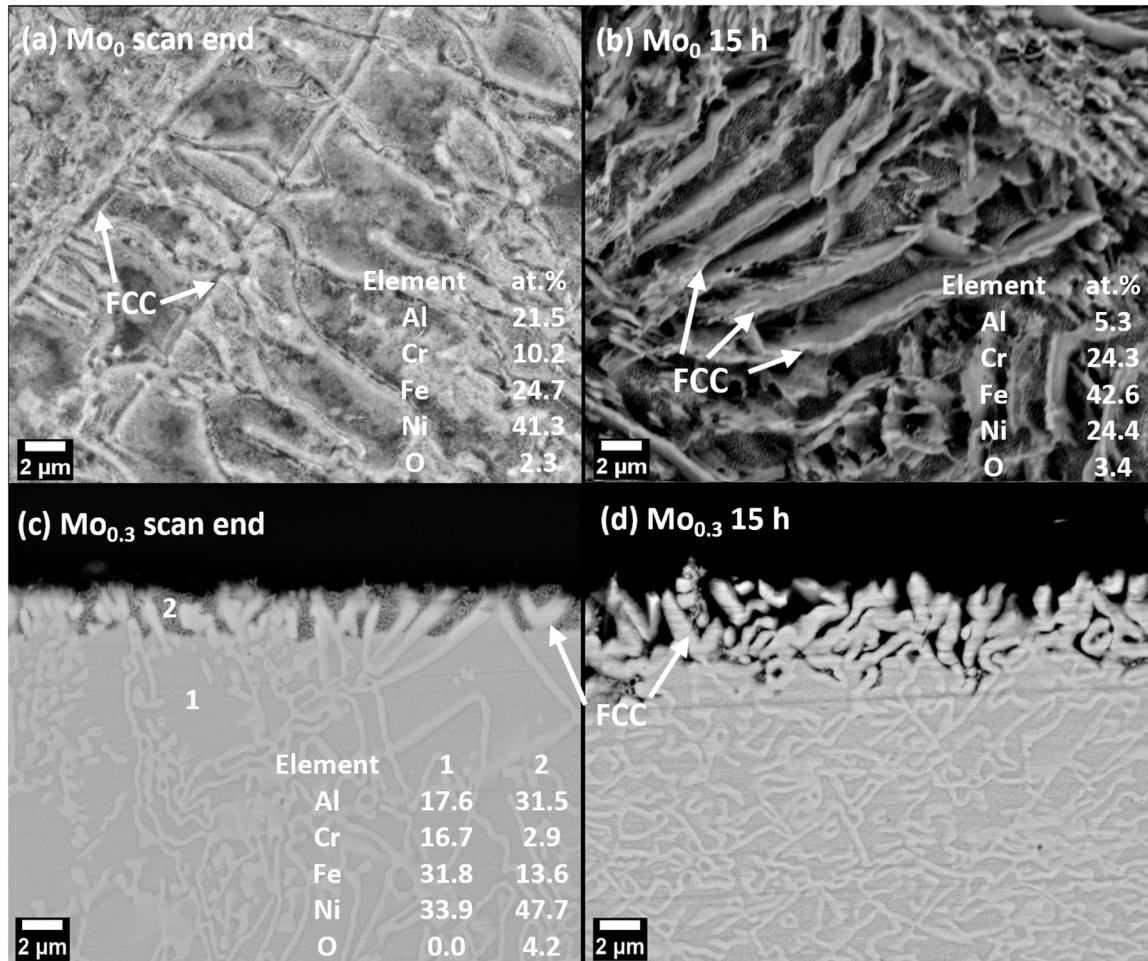


Fig. 6. Typical BSE images of Mo_0 surfaces (a, b) and cross-sections (c, d). Images (a, c) were taken at CPP scan end, while images (b, d) after additional 15 h of immersion. Inserted tables show average chemical compositions of scanned areas (a, b), while points 1 and 2 in (c) mark the locations of EDS spot analysis.

employed to compare topography during the CPP test, and surface composition at scan end for three alloys: Mo₀, Mo_{0.3} and Mo_{0.6}. The initial images of these specimens as-immersed in 0.1 M H₂SO₄ are presented in Fig. 7a, (Fig. 8) a and a, respectively. During polarisation, the Mo₀ surface remained relatively stable, whereas certain features such as grain boundaries, initially visible, became more and more hazed with the increasing applied potential (Fig. 7). Only in the transpassive region did the surface roughness increase as evidenced by the AFM image, and the AFM height profiling. Locations of the grain boundaries, which coincide with the FCC phase, are indicated by dotted lines. The EDS analysis Fig. 9 at the scan end displays an inhomogeneous surface, with Al and Ni dominating on the joint map. The slight segregation of Cr and Fe can also be discerned near the grain boundaries.

For Mo_{0.3}, the onset of corrosion changes is visible as a slight increase in surface roughness upon polarisation, evidenced by the AFM height profiles (Fig. 9b). In the region of transpassive potentials (Fig. 9c) significant differences in the height profile can be noticed. SEM and EDS analyses at the CPP scan end (Fig. 10) revealed depletion of Mo, and to a lesser extent of Cr, in the grain boundary region. This stays in contrast to the initial enrichment of the grain boundaries in these elements (Fig. 3a). Moreover, the bright areas along the grain boundaries in the AFM image are rich in Al and Ni.

Upon further inspection of the Mo_{0.3} surface after scan end, by means of secondary electron (SE) and BSE detectors, it turned out that the area scanned by the AFM cantilever had different topography compared with the surroundings (Fig. 11). This is distinctly visible in the SE image in (a). Similar effects were not observed on the surface of Mo₀. A plausible explanation is that the relatively dense network of the FCC phase on the surface of Mo₀ (Fig. 6), prevented deformation of the passive layer over

the spinodally decomposed area upon scanning with the AFM cantilever. Such support was not possible in the case of Mo_{0.3}, which lacks the FCC phase (Fig. 1). As a result, the surface roughness of Mo_{0.3} increased markedly, which is reflected in much larger height differences between the surface of Mo_{0.3} and Mo₀ (555 nm vs 150 nm, respectively) in the transpassive state. In particular, the insides of the grains seem to have changed the most in terms of height, as can be seen in Figs. 9c and 11a. This might also affect the distribution of elements observed with EDS in Fig. 10. Therefore, the results of AFM height profiling in the areas of spinodal decomposition should be interpreted with caution (Fig. 12).

In the case of Mo_{0.6}, the BCC-B2 grains were bigger compared with the elements of spinodally decomposed microstructure, which made them easier to track with AFM during polarisation (Fig. 12). In the initial state they could be recognized as bright spots (Fig. 12a), which became dark in the passive region (Fig. 12b). The height profiling scanline crossing one of the BCC-B2 grains showed a depression of about 150 nm (Fig. 12b). In the transpassive region the surface roughness increased (Fig. 12c), but positions of the BCC-B2 grains were not clear. However, the SEM image and EDS mapping of the surface in Fig. 13 revealed, that the BCC-B2 grains were still present on the surface. Similarly, EDS maps confirmed the Al and Ni enrichment in the areas of spinodal decomposition. The surface composition of Mo_{0.6} was much less uniform compared with Mo₀, with distinct (Al, Ni)-rich and (Fe, Cr, Mo)-rich domains not always corresponding to the microstructural features observed on SEM images.

3.4. Properties of passive films

As the CPP curves indicated the occurrence of passive films in a wide

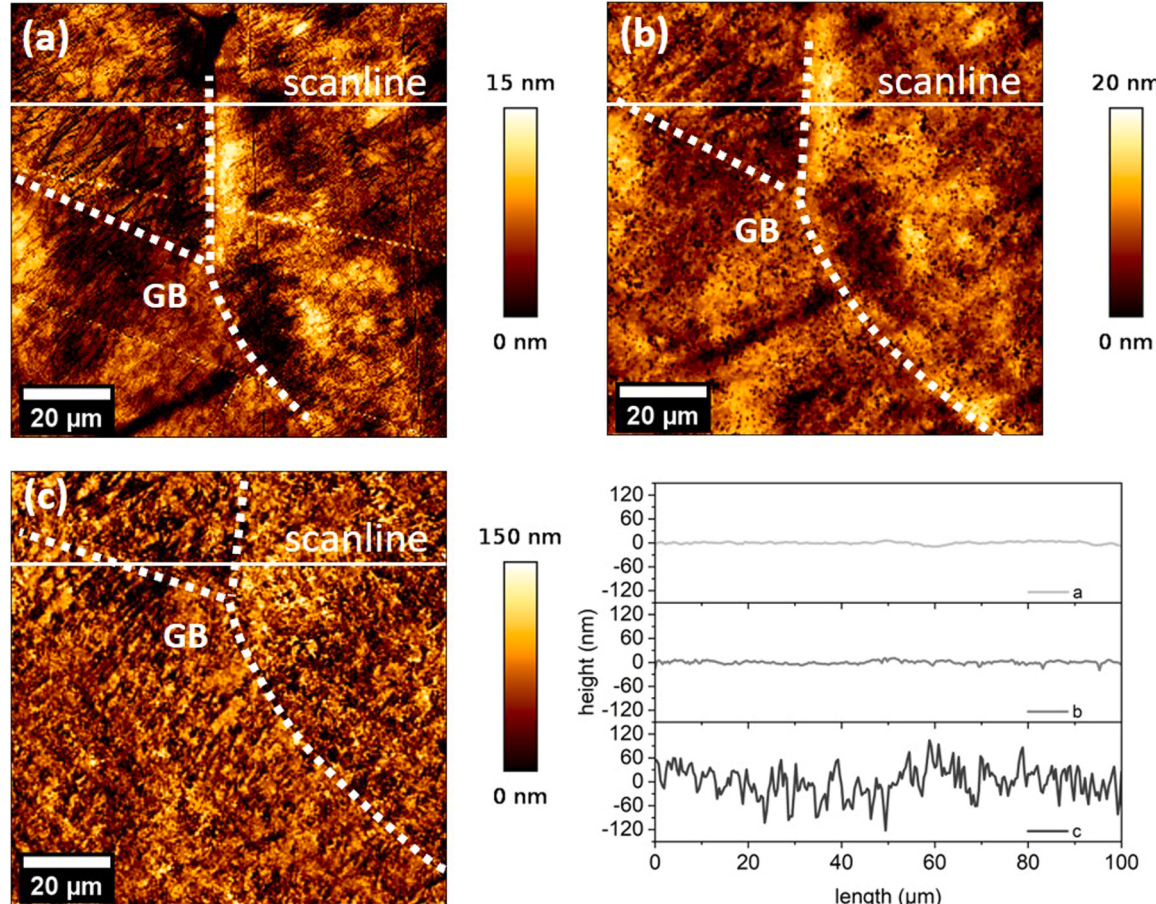


Fig. 7. AFM images of the Mo₀ surface (a) as-immersed, (b) during polarisation in the passive region and (c) in the transpassive region (5 mA). Dotted lines illustrate grain boundaries (GB), which coincide with the locations of FCC phase. The diagram summarizes respective height profiles along the indicated scanlines.

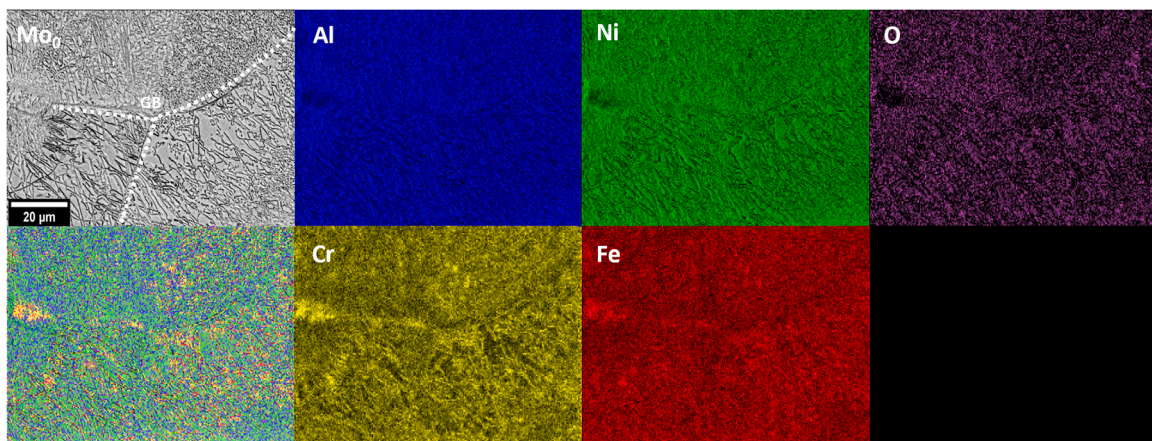


Fig. 8. BSE image and EDS maps of the Mo_0 surface at the CPP scan end. Dotted lines illustrate grain boundaries (GB), which coincide with the locations of FCC phase.

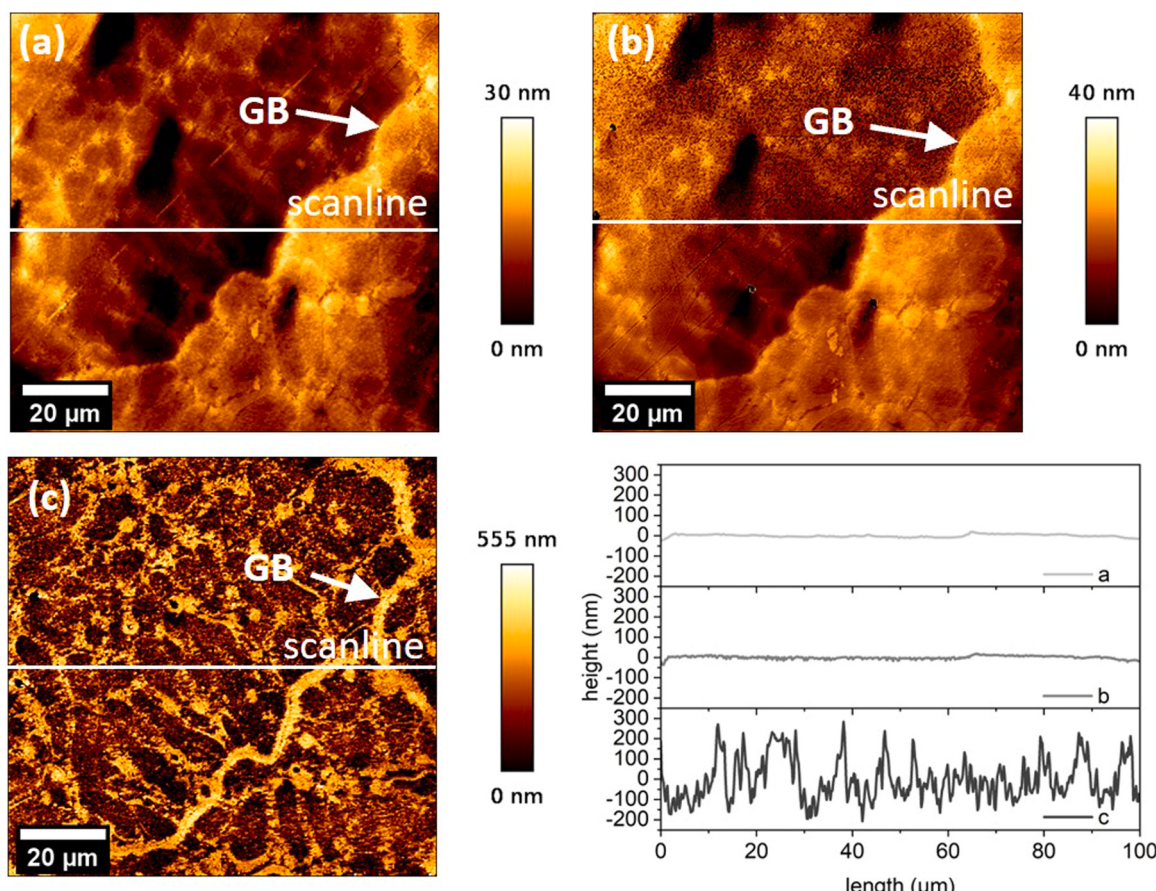


Fig. 9. AFM images of the $\text{Mo}_{0.3}$ surface (a) as-immersed, (b) during polarisation in the passive region (5 mA), and (c) in the transpassive region (5 mA), with the arrows pointing at the grain boundaries (denoted as GB). The diagram summarizes respective height profiles along the indicated scanlines.

range of potential, we decided to monitor changes in current density during 2-h potentiostatic polarisation at 0.6 V_{SCE}. The results are presented in Fig. 14. Except for $\text{Mo}_{0.6}$, which exhibited higher current densities over the entire time span, all alloys behaved in a very similar manner – after an initial fast decrease, the curves flattened out to approach current densities of less than $1.0 \mu\text{Acm}^{-2}$, and finally below $0.5 \mu\text{Acm}^{-2}$ after 2 h, i.e. remarkably less compared with i_{pass} recorded in the CPP experiments (Fig. 4).

To assess the passivation behaviour of $\text{AlCrFe}_2\text{Ni}_2\text{Mo}_x$ alloys, samples were polarised at a potential of 0.6 V_{SCE} for 2 h (Fig. 14) and

subsequently analysed by EIS. The results are presented in the Nyquist and Bode plots in Fig. 15 with an electrical equivalent circuit (EEC) used for experimental data fitting, inserted in Fig. 15a. The measured points in the Nyquist plot all form unfinished semicircles, which indicates similar passivation mechanisms. The Bode plot shows a linear relationship between $\log |Z|$ and $\log |f|$ in the 10^{-2} to 10^3 Hz frequency range. The maximum values of phase angle are lower than 90 degrees, indicating pseudocapacitive behaviour [73]. Both Nyquist and Bode plots confirm very similar behaviour of all investigated alloys, except $\text{Mo}_{0.6}$, for which the depressed semicircle in Fig. 15a is much smaller

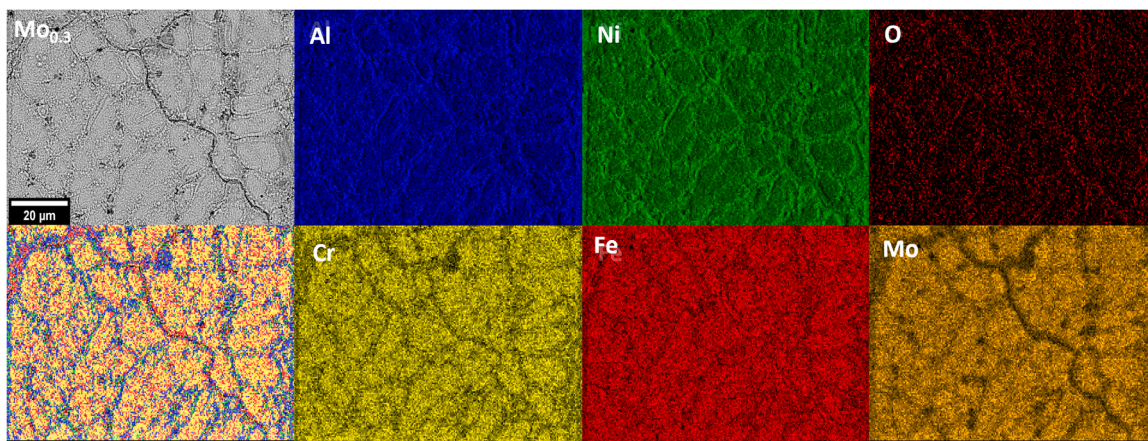


Fig. 10. BSE image and EDS maps of $\text{Mo}_{0.3}$ at the CPP scan end. Images are rotated 90 degrees counterclockwise with respect to AFM images in Fig. 9.

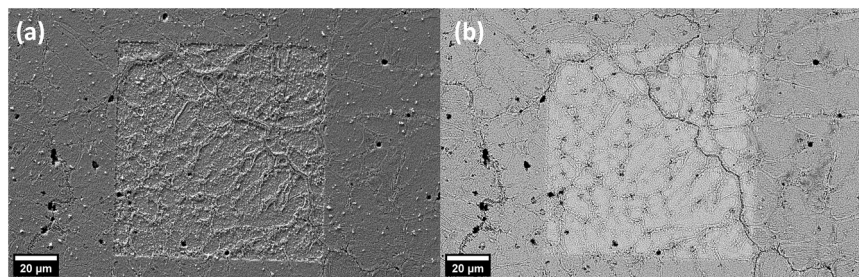


Fig. 11. (a) SE and (b) BSE images of the $\text{Mo}_{0.3}$ surface at the CPP scan end, showing the area deformed by the AFM cantilever.

and the phase angle on the Bode plot is visibly lower at low frequencies.

The EEC chosen to fit the experimental data is typical of alloys producing non-uniform two-layer passive films [35], [74], [75] and consists of a solution resistance (R_s), an electrical resistance and capacitance of the outer layer (R_1 and Q_1 , respectively), and electrical resistance and capacitance of the inner layer (R_2 and Q_2 , respectively). Capacitance in both cases is represented by a constant phase element (CPE) to take account of the heterogeneity of impedance distributions [27], [76]. It is described as $\text{CPE} = [Q \ (\text{i}\omega)^n]^{-1}$, where Q is the capacitance, $i = (-1)^{0.5}$, ω is the angular frequency and n is the value between -1 (for an inductor) and 1 (for a capacitor), while $n = 0$ represents a resistor and $n = 0.5$ a diffusion element [77]. The EEC fitting parameters are listed in Table 5. The fitted values show that the outer layer was much more compact ($n_1 = 1$ for all alloys) and had much better corrosion resistance ($R_1 > 100 \text{ k}\Omega\text{cm}^2$), compared with the inner layer (n_2 of around 0.85 and R_2 of around $10 \text{ k}\Omega\text{cm}^2$).

The R_1 values increase with Mo content up to $\text{Mo}_{0.3}$, while changes in R_2 values are inconsistent. Overall, the contribution to the overall corrosion resistance at $0.6 \text{ V}_{\text{SCE}}$ are relatively low ($R_1 \gg R_2$). Although, the resistance of the outer layer in $\text{Mo}_{0.6}$ is lower, and that of the inner layer is higher compared with other alloys, the value of R_1 is still few times higher than R_2 ($105 \text{ k}\Omega\text{cm}^2$ vs. $17.1 \text{ k}\Omega\text{cm}^2$). The corresponding values of capacitance (Q_1 and Q_2) are lower for $\text{Mo}_{0.6}$ than for other alloys.

The polarisation experiments were complemented by AFM imaging (Fig. 16). To monitor differences in the passivation ability of alloys with various Mo concentrations, the surfaces of $\text{Mo}_{0.3}$ and $\text{Mo}_{0.6}$ were examined in the as-immersed state (Fig. 16a and d), after 1-h polarisation at $0.4 \text{ V}_{\text{SCE}}$ (Fig. 16b and e) and after 2-h polarisation at $0.4 \text{ V}_{\text{SCE}}$ (Fig. 16c and f). The images of $\text{Mo}_{0.3}$ in Fig. 16a, b and c indicate that during polarisation its surface underwent little to no change. The relative height difference decreased by as little as 5 nm - from 40 nm to 35 nm . In contrast, those for $\text{Mo}_{0.6}$ changed from 26 nm in the as-immersed state, to 62 nm after 2 h of polarisation, and locations of the

BCC-B2 phase, distinguishable as bright spots in Fig. 16d, darkened with time, signifying their selective dissolution, similarly as in Fig. 12.

Finally, the passivation kinetics of $\text{Mo}_{0.3}$ and $\text{Mo}_{0.6}$ was evaluated from 1-h potentiostatic polarisation tests at the passive potential of $0.4 \text{ V}_{\text{SCE}}$, with reference to the high-field model assuming that at an early stage the film formation and growth is exclusively a result of ionic conduction and species migration across the film under a high electric field. In this model the current density generated during the passivation process depends on time and charge density according to the following equations [78]–[79]:

$$\log(i) = \log A_1 - n \log(t) \quad (1)$$

$$\log(i) = \log A_2 + \frac{cBV}{q(t)} \quad (2)$$

where $i(t)$ is the current density, t is the time, A_1 is a constant, and n is the passivation index which can indirectly express growth rate of the passive film, $q(t)$ is the charge density, A_2 and B are parameters associated with the energy of activation for charges displacement, V is the potential drop across the passive film and c is a constant related to the film. To apply these equations, the $\log i(t)$ vs. $q(t)$ plot was drawn (Fig. 17a) and the initial linear ranges were found which usually cannot be described by the high-field model. The $\log i(t)$ vs. $\log t$ and $\log i(t)$ vs. $1/q(t)$ plots in Fig. 17b and c, respectively, were used to evaluate the n and cBV parameters representing the passivation behaviour [80]. The passivation indices, n , determined from the plots in Fig. 17b have the same value (0.86) for both alloys. This value falls exactly in the range $0.80 - 0.95$, which is usually considered sufficiently high to justify the use of Eq. 2 [81]. On the other hand, the cBV values determined from the plot in Fig. 17c are different: 0.86 Ccm^{-2} for $\text{Mo}_{0.3}$ and 1.26 Ccm^{-2} for $\text{Mo}_{0.6}$, which translates to the higher activation energy of the passive film formation, and therefore worse passivation properties of $\text{Mo}_{0.6}$ [79].

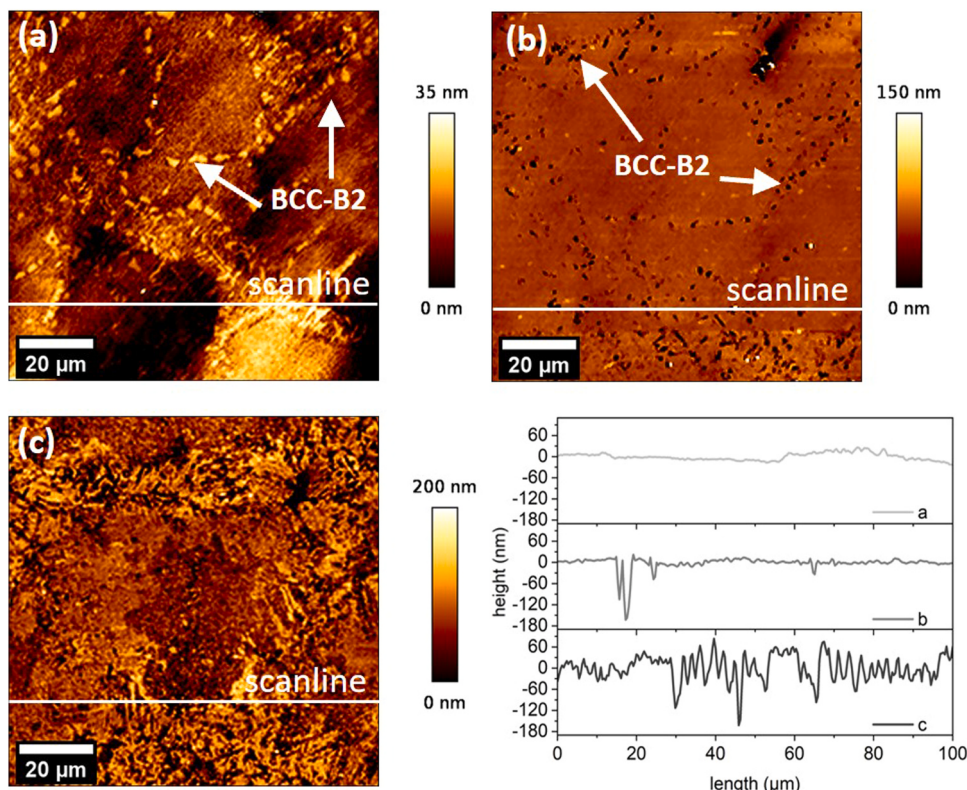


Fig. 12. AFM images of the Mo_{0.6} surface a) as-immersed, b) during polarisation in the passive region and c) during polarisation in the transpassive region (5 mA), with the arrows pointing at the BCC-B2 phase. The diagram summarizes the respective height profiles along the indicated scanlines.

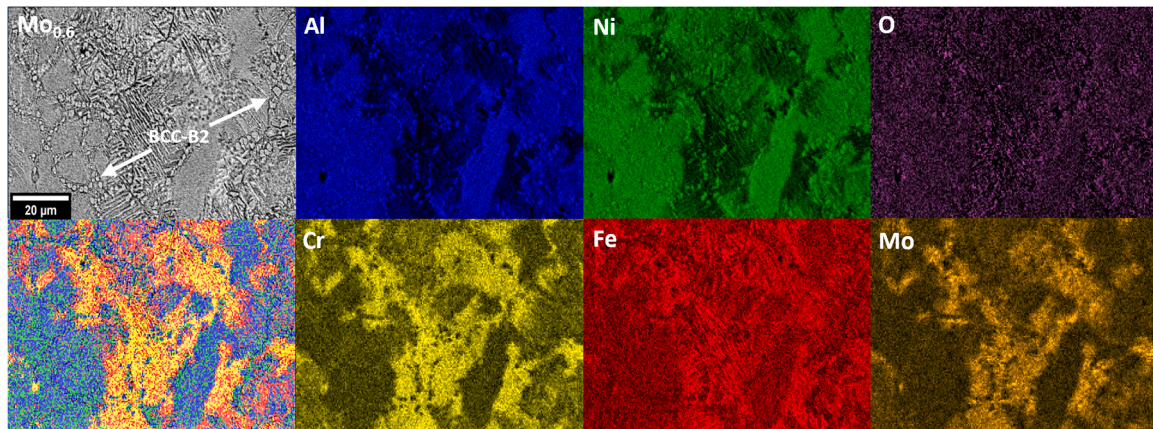


Fig. 13. BSE image and EDS maps of Mo_{0.6} at the CPP scan end.

4. Discussion

Although various techniques were employed for the analysis of AlCrFe₂Ni₂Mo_x alloys surfaces in polarised and unpolarised states (0.4 V, 5 mA, CPP scan end, 15 h), the results were not clear enough to draw conclusions about the reactions mechanisms. Therefore, additional CPP experiments were done using pure metals and intermetallic compounds to seek similarities with the investigated alloys. Selected results for Al, Ni, equimolar NiAl and Cr are shown in Fig. 18.

It can be seen that the active dissolution stage of AlCrFe₂Ni₂Mo_x alloys in Fig. 18 resembles those of Ni and NiAl, while Al and Cr exhibit spontaneous passivation. Therefore, the initial part of the CPP curves for

the investigated alloys is apparently associated with dissolution of the BCC-B2 phase and Fe, which is known to readily dissolve in the pre-passive state [41], [82]. This statement can be supported by the AFM images in Fig. 12a and b, which show that pits on the surface of Mo_{0.6} upon reaching the passive region appeared in the initial location of the BCC-B2 grains and by relatively high concentrations of Al, Ni and Fe in the solutions at 0.4 V (Table 4).

The passivation range of AlCrFe₂Ni₂Mo_x alloys extends from 0.0 to 0.8 V_{SCE}. According to XPS analyses (Table 3), Al, Cr and Fe exhibit the strongest tendencies to form the oxidized forms in the passive film at 0.4 V. The EEC derived from the EIS measurements (Fig. 15, Table 5) indicates the occurrence of a two-layer passive film, consisting of a

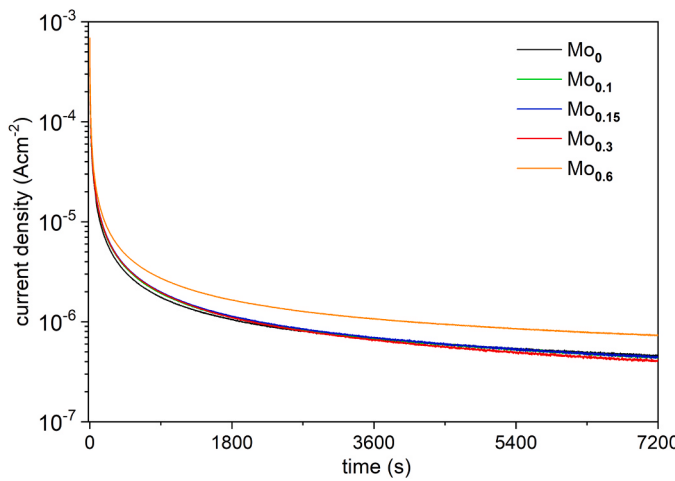


Fig. 14. Current densities of $\text{AlCrFe}_2\text{Ni}_2\text{Mo}_x$ alloys during 2-h polarisation at $0.6 \text{ V}_{\text{SCE}}$ in $0.1 \text{ M H}_2\text{SO}_4$.

compact outer layer ($n_1 = 1$) and a less compact inner layer ($n_2 \approx 0.85$) with much lower corrosion resistance ($R_1 >> R_2$). The Al oxides/hydroxides are known to form more porous and thicker films than those composed of Cr^{3+} species [21], [71], [83]. Therefore, it can be assumed that the outer compact layer consists mainly of Cr, Fe and Mo species, while the inner porous one is mainly composed of Al species. A similar structure was proposed in [82] for the passive film grown on Al-27Cr-8Fe polarised in $1 \text{ M H}_2\text{SO}_4$, mostly composed of aluminium oxy-hydroxides and enriched in Cr in the outermost part. Akiyama et al. who studied the corrosion behaviour of Al-36Cr-9Mo [84] attributed this structure to the faster dissolution and slower migration of aluminium cations in the passive film, compared with chromium cations. It is worth noting, that in both mentioned cases a concentration gradient model of the passive film was proposed, although the Al concentration in investigated alloys was considerably higher than that of Cr. The approximate thicknesses of the oxide layers formed on $\text{AlCrFe}_2\text{Ni}_2\text{Mo}_x$ alloys in the bilayer model proposed in this work were calculated from Eq. (3), according to [85]:

$$C_{\text{eff}} = \frac{\varepsilon \varepsilon_0}{d_{\text{oxide}}} \quad (3)$$

where C_{eff} is effective oxide film capacitance measured at f_{max} (the frequency at which the most negative phase angle value was observed [86]), d_{oxide} is oxide film thickness, ε_0 is vacuum permittivity equal to $8.854 \times 10^{-14} \text{ F cm}^{-1}$ and ε is relative permittivity of the passive film. Although ε value is not known for passive films on $\text{AlCrFe}_2\text{Ni}_2\text{Mo}_x$,

alloys, it could be taken as 10 [87] for the inner layer composed mainly of Al-containing species, as Al_2O_3 is the prevailing Al compound in the passive films on $\text{Al}(\text{Co})\text{CrFeNi}$ alloys in various solutions [15], [20], [71]. For the outer layer, the value of ε was assumed as 12, which is typical of Cr- and Fe-based passive films on HEAs [72], [88] and stainless steels [89]. The corresponding capacitance values were determined for the inner layer of the passive film on each alloy with Eq. (4) [85]:

$$C_{\text{eff}} = Q_{\text{eff}} (2\pi f_{\text{max}})^{n-1} g, \text{ where } g = 1 + 2.88 (1 - n)^{2.375} \quad (4)$$

When $n = 1$, as in the case of the outer layer, the CPE coefficient (Q_{eff}) becomes capacitance ($Q_{\text{eff}} = C_{\text{eff}}$) [90]. Some authors [71], [91], [92] also used another equation to determine thickness of the passive film, where R_f is a passive film resistance:

$$C_{\text{eff}} = \frac{(Q_{\text{eff}} \cdot R_f)^{1/n}}{R_f} \quad (5)$$

The values received from Eq. (4) and Eq. (5) differed by less than 10%, which proves correctness of the assumed model. The calculated values of film capacitance C_{eff} and thickness d_{oxide} are given in Table 6. Small additions of Mo (0.1 and 0.15) led to decrease in thickness of both oxide films. More elevated additions of Mo resulted in an increase in d_{oxide} , with a very distinct thickening of the passive layers on $\text{Mo}_{0.6}$. The passive film on this alloy consisted of a slightly thicker Cr-based layer and almost twice thicker Al_2O_3 layer, compared with other alloys. However, the thicker outer layer on $\text{Mo}_{0.6}$ was still much less protective than on other alloys. This can be supported by in-situ AFM images (Fig. 16d-f), which show progressive dissolution of the BCC-B2 grains in $\text{Mo}_{0.6}$, compared with successful passivation of $\text{Mo}_{0.3}$ (Fig. 16a-c). Similar tendencies could be derived from the analysis of passivation kinetics based on the high-field model. The passivation index n of 0.86 for both alloys would testify to rapid kinetics. However, the distinctly higher value of the cBV parameter for $\text{Mo}_{0.6}$ compared with $\text{Mo}_{0.3}$ (Fig. 17c) denotes worse passivation ability linked to high activation energy for the transfer of charges and ions through the film. The cBV parameter is also interpreted in terms of susceptibility of the film to stress corrosion cracking (SCC), i.e. cyclic film breakdown-dissolution-repassivation: the higher its value, the lower resistance to SCC. By comparing the cBV values for $\text{Mo}_{0.3}$ and $\text{Mo}_{0.6}$ we can expect that $\text{Mo}_{0.6}$ is more susceptible to SCC than $\text{Mo}_{0.3}$. The cBV value is apparently related to chemical composition, thickness and compactness of the passive film: namely, thin and defect-free films are characterized by small values of cBV [80], [79], which coincides with the results presented in this work.

The transpassive region starting from $0.8 \text{ V}_{\text{SCE}}$ on the CPP curve (Fig. 4) is apparently connected with the change in the oxidation state of chromium from Cr(III) to (VI) and the appearance of $\text{Cr}_2\text{O}_7^{2-}$ ions in the

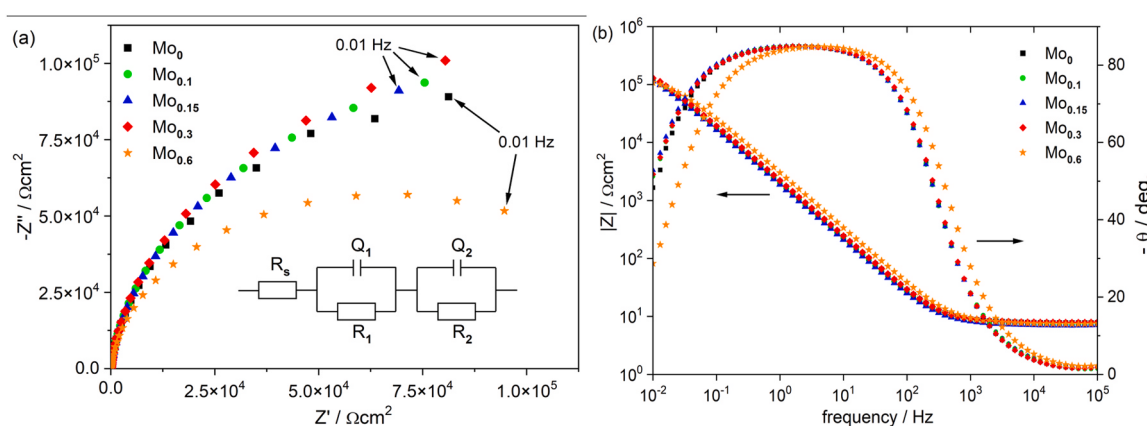


Fig. 15. Nyquist (a) and Bode (b) plots of $\text{Mo}_0 - \text{Mo}_{0.6}$ alloys after 2-h polarisation at $0.6 \text{ V}_{\text{SCE}}$ in $0.1 \text{ M H}_2\text{SO}_4$. Corresponding fitted electrical equivalent circuit is inserted in Fig. 15a.

Table 5

Equivalent circuit parameters fitted for AlCrFe₂Ni₂Mo_x alloys polarised at 0.6 V_{SCE} in 0.1 M H₂SO₄.

Alloy	R _s ($\Omega \text{ cm}^2$)	Q ₁ ($\Omega^{-1} \text{ cm}^{-2} \text{s}^n \times 10^{-6}$)	n ₁ (-)	R ₁ ($\text{k}\Omega \text{ cm}^2$)	Q ₂ ($\Omega^{-1} \text{ cm}^{-2} \text{s}^n \times 10^{-6}$)	n ₂ (-)	R ₂ ($\text{k}\Omega \text{ cm}^2$)
Mo ₀	7.6 ± 0.5	58.9 ± 6.4	1.00 ± 0.00	175 ± 4	18.6 ± 0.6	0.86 ± 0.01	10.5 ± 0.6
Mo _{0.1}	7.5 ± 0.7	60.6 ± 11.2	1.00 ± 0.00	184 ± 24	21.6 ± 2.6	0.85 ± 0.01	8.6 ± 0.7
Mo _{0.15}	7.3 ± 0.7	62.4 ± 9.0	1.00 ± 0.00	180 ± 4	19.7 ± 1.9	0.85 ± 0.01	9.9 ± 0.5
Mo _{0.3}	7.7 ± 0.6	55.5 ± 8.4	1.00 ± 0.00	206 ± 15	16.2 ± 2.4	0.86 ± 0.01	11.9 ± 1.1
Mo _{0.6}	7.6 ± 0.9	48.1 ± 7.9	1.00 ± 0.00	105 ± 2	9.2 ± 1.8	0.89 ± 0.02	17.1 ± 4.9

electrolyte [93]. This leads to gradual dissolution of the outer part of passive film, leaving behind an inner Al₂O₃ layer and the surface enriched in Ni species, which at high potentials could be readily oxidised, as evidenced at 5 mA by XPS (Table 3).

During the reverse scan, current densities of AlCrFe₂Ni₂Mo_x alloys were lower compared with the forward scan. Similar behaviour of a CoCrFeMnNi in a H₂SO₄ solution, reported by Wetzel et al. [58], was interpreted as stronger passivation due to the higher available concentrations of oxygen, which accumulated close to the electrode surface during polarisation at very high anodic potentials. In our studies, the decreased current densities were noticed during the reverse scan in the case of Cr and NiAl (Fig. 18). Since Al³⁺, Ni²⁺ and Cr³⁺ ions dominated on the surface of alloys at 5 mA (Table 3), it is possible that two processes contribute to the decrease in current densities: fast recovery of the Cr-based passive film due to the absence of iron on the surface, and enrichment of the passive film in Ni²⁺, which in combination with Al³⁺ can form an effective passive film on NiAl, as evidenced by CPP in Fig. 18.

At the end of cyclic polarisation scan the surface of Mo₀ was enriched in Al and Ni (Fig. 6a), which is similar to its state at 5 mA indicated by XPS. Moreover, the cross sections in Fig. 6c revealed, that the composition of the corroded area corresponds to the composition of BCC-B2 reported in [12]. From these results, it can be derived that within the spinodal decomposition area the BCC-A2 phase is the first to react: similar conclusions were drawn by Xiang et al. [25] who studied corrosion behaviour of AlCoCrFeNiSi_{0.1} and observed dissolution of (Cr, Fe)-rich precipitates rather than the (Al, Ni)-rich matrix in the

transpassive region, although in their work no reverse scan was conducted. The additional 15-h immersion after scan end led to a significant decrease in the Al and Ni concentrations (Fig. 6b). The cross-section in Fig. 6d shows that the only phase still present at the surface was FCC, and that BCC-B2 was almost entirely leached out. The protective films, formed on the surface of alloys during CPP, dissolved within a few hours of immersion without external polarisation and could not recover. This explanation is supported by the ICP analyses of the solutions (Table 4), which show much higher concentrations of ions, in particular Al, Ni and Fe, at 15 h compared with the scan end. These results do not coincide with the opinions of other authors claiming selective dissolution of the BCC-B2 phase regardless of the polarisation conditions [22], [23]. Therefore, more research is still needed to unravel the passivation mechanisms of Al(Co)CrFeNi alloys in H₂SO₄.

The addition of Mo in small amounts, up to Mo_{0.15}, changed the microstructures and phase compositions of AlCrFe₂Ni₂Mo_x alloys only to a small extent. Fractions of the FCC phase successively decreased, making the surface more homogeneous. This tendency was maintained in the case of Mo_{0.3} as well, but was accompanied by Mo enrichment along the grain boundaries (Fig. 3). High amount of Mo in Mo_{0.6} triggered formation of the σ phase (Fig. 1) and segregation of Al and Ni into separate BCC-B2 grains (Figs. 2 and 3). Moderate amounts of Mo were beneficial for passivation of AlCrFe₂Ni₂Mo_x alloys during anodic polarisation in 0.1 M H₂SO₄, as indicated by very low current densities (below 0.5 μAcm^{-2}) after 2-h polarisation (Fig. 14) and by the EEC fitting parameters in Table 5. Although the inner and outer layers of the passive films were thinner in Mo_{0.1} and Mo_{0.15} compared with Mo₀

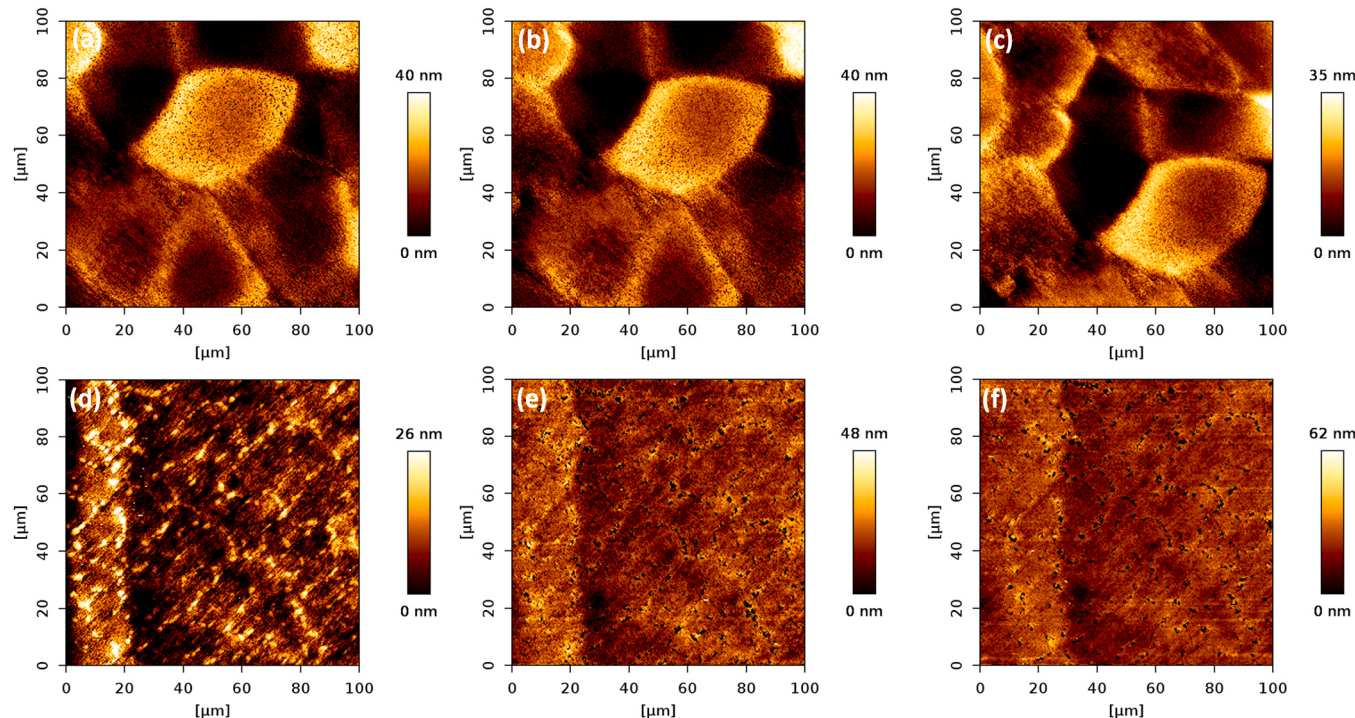


Fig. 16. AFM images of the Mo_{0.3} surface (a) as-immersed, (b) after 1-h polarisation at 0.4 V_{SCE}, (c) after 2-h polarisation at 0.4 V_{SCE} and the Mo_{0.6} surface (d) as-immersed, (e) after 1-h polarisation at 0.4 V_{SCE}, (f) after 2-h polarisation at 0.4 V_{SCE}.

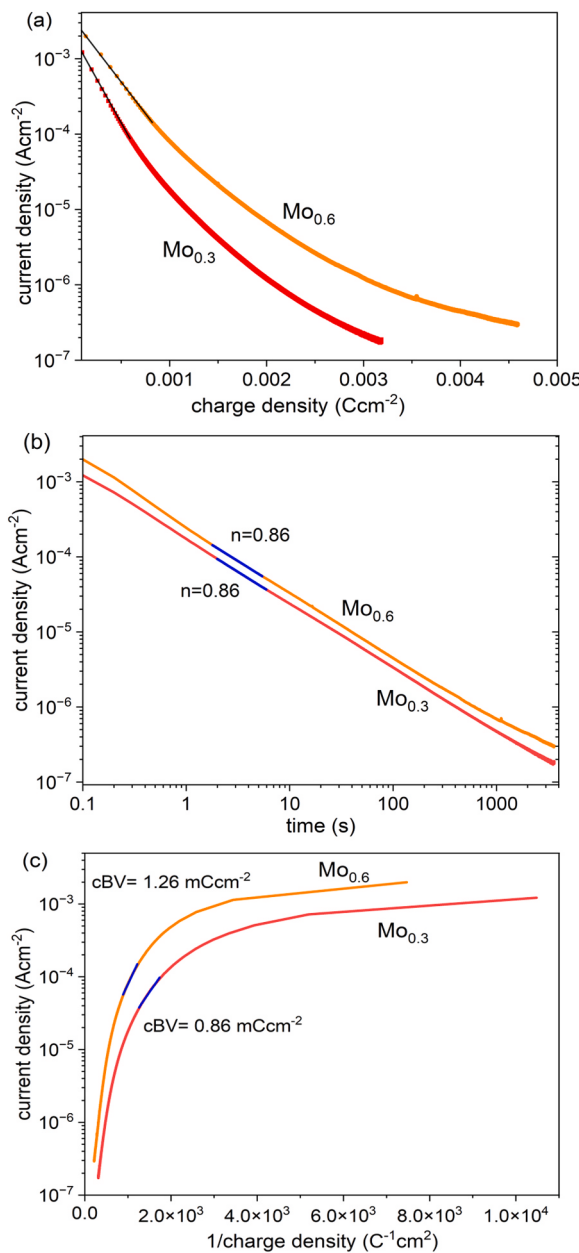


Fig. 17. Plots representing 1-h potentiostatic passivation of alloys $\text{Mo}_{0.3}$ and $\text{Mo}_{0.6}$ at $0.4 \text{ V}_{\text{SCE}}$: (a) log current density vs charge density, (b) log current density vs log time and (c) log current density vs $1/\text{charge density}$. Black lines in (a) indicate linear dependence between i and q , while blue lines in (b) and (c) indicate linear fits used to determine passivation indices n and cBV , respectively, according to high-field model.

(Table 6), the resistance of their Cr-rich outer layer was still slightly higher. This improvement can be attributed to the increased stabilization of the Cr^{3+} species in the passive film, due to the Mo-promoted deprotonation of $\text{Cr}(\text{OH})_3$ to Cr_2O_3 [37], [38], [66]. Thickness of the passive film on $\text{Mo}_{0.3}$ was the same as on Mo_0 but its resistance was the highest among $\text{AlCrFe}_2\text{Ni}_2\text{Mo}_x$ alloys. Some authors [35], [38], [94] suggested, that the well-adjusted Cr/Mo concentration ratios can bring about a synergistic effect manifested by a markedly improved passivation ability. That would explain, why the amount of Cr^{3+} ions indicated by XPS at 5 mA was twice higher for $\text{Mo}_{0.3}$ than for Mo_0 (Table 3), and why the concentrations of ions in the solutions detected by ICP-OES during the CPP scan (Table 4) were lower for $\text{Mo}_{0.3}$ than for Mo_0 . Importantly, the passivation properties of $\text{Mo}_{0.3}$ were the best despite

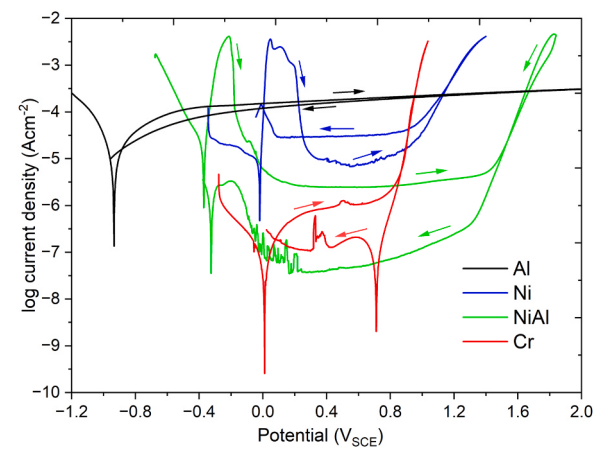


Fig. 18. Cyclic potentiodynamic polarisation curves of Al, Ni, NiAl and Cr in $0.1 \text{ M H}_2\text{SO}_4$ solution on the same setup as for $\text{AlCrFe}_2\text{Ni}_2\text{Mo}_x$ alloys.

Table 6

Calculated values of capacitance and thickness of the outer and inner oxide layers.

Alloy	outer layer (Cr_2O_3)		inner layer (Al_2O_3)	
	$C_{\text{eff}} \times 10^{-5}$ [Fcm^{-2}]	d_{oxide} [nm]	$C_{\text{eff}} \times 10^{-5}$ [Fcm^{-2}]	d_{oxide} [nm]
Mo_0	5.89	0.19	1.32	0.70
$\text{Mo}_{0.1}$	6.06	0.18	1.51	0.59
$\text{Mo}_{0.15}$	6.24	0.17	1.42	0.63
$\text{Mo}_{0.3}$	5.55	0.19	1.17	0.77
$\text{Mo}_{0.6}$	4.81	0.22	0.65	1.38

Mo segregation to the grain boundaries. On the other hand, the corrosion resistance of $\text{Mo}_{0.6}$ was visibly worse compared with other investigated alloys. The less homogeneous distribution of phases on the surface of $\text{Mo}_{0.6}$ promoted selective corrosion of the BCC-B2 phase at the initial stages of polarisation (Fig. 12a and b, Fig. 16d-f) and hindered the formation of a passive film. It was evidenced by the worse performance of this alloy in all electrochemical tests, despite both layers of the passive film thicker than on other alloys (Table 6).

5. Conclusions

The key conclusions from the investigations on the influence of Mo on the microstructure and corrosion behaviour of $\text{AlCrFe}_2\text{Ni}_2\text{Mo}_x$ alloys in $0.1 \text{ M H}_2\text{SO}_4$ carried out in this work can be summarized as follows:

- with the increasing concentration of Mo, the fraction of FCC phase in $\text{AlCrFe}_2\text{Ni}_2\text{Mo}_x$ alloys gradually decreased. In Mo_0 , $\text{Mo}_{0.1}$ and $\text{Mo}_{0.15}$, three phases: FCC, BCC-A2 and BCC-B2 were identified, but $\text{Mo}_{0.3}$ contained BCC-A2, BCC-B2 and very small amount of σ phase. In $\text{Mo}_{0.6}$, which showed significant segregation of elements, the amount of σ phase was more pronounced;
- Mo at concentrations of up to 5 at% ($\text{Mo}_{0.3}$) had a positive effect on the protective properties of the passive films. Its further increase to 9.6 at% ($\text{Mo}_{0.6}$) was detrimental;
- under the open-circuit conditions, the dominating corrosion process was selective corrosion of the (Al, Ni)-rich BCC-B2 phase. However, in the conditions of external polarisation, passive films developed on the surface changed the corrosion mechanism and led to a significant decrease in current densities;
- the passive films, built of an outer layer, mostly composed of Cr-, Fe- and Mo-containing species, and an inner layer, composed of Al-containing species, had good protective properties. Upon cyclic

- potentiodynamic sweep, the (Cr, Fe, Mo)-rich BCC-A2 phase was the most active in the development of passive films;
- although the (Cr, Fe, Mo)-rich outer layer of the passive films dissolved in the transpassive potential range ($>0.8 \text{ V}_{\text{SCE}}$), it quickly recovered during the reverse scan, as evidenced by lower current densities compared with the forward scan;
 - the Mo_{0.3} composition appeared the most promising, owing to the synergistic effect of Cr and Mo on the development of passive films with good protective properties.

CRediT authorship contribution statement

Mitoraj-Krolikowska Marzena: Writing – review & editing, Validation, Methodology, Investigation, Conceptualization. **Godlewska Elzbieta:** Writing – review & editing, Supervision, Resources. **Czerski Jakub:** Writing – original draft, Visualization, Validation, Methodology, Investigation, Formal analysis, Conceptualization. **Wetzel Annica:** Writing – review & editing, Investigation, Formal analysis. **Witt Julia:** Supervision. **Ozcan Ozlem:** Supervision, Resources. **Marzec Mateusz:** Investigation. **Goly Marcin:** Investigation.

Declaration of Competing Interest

The authors declare that they have no known competing financial interests or personal relationships that could have appeared to influence the work reported in this paper.

Data Availability

Data will be made available on request.

Acknowledgements

The authors acknowledge the contribution of Sergej Gein from the Access e.V. Aachen, who manufactured all alloys analysed in this paper. Investigations were conducted within a NADEA project (M-ERA.NET 2017) with a financial support from the National Science Centre Poland (UMO-2017/26/Z/ST8/ 01238) and subsidy of the Ministry of Education and Science for the AGH University of Krakow (Project No 16.16.160.557). Research project was also partly supported by program 'Excellence initiative – research university' for the University of Krakow.

References

- [1] M. Tokarewicz, M. Grądzka-Dahlke, Review of recent research on AlCoCrFeNi high-entropy alloy, Met. (Basel) vol. 11 (8) (2021), <https://doi.org/10.3390/met11081302>.
- [2] Y. Lu, et al., A promising new class of high-temperature alloys: eutectic high-entropy alloys, Sci. Rep. vol. 4 (2014) 1–5, <https://doi.org/10.1038/srep06200>.
- [3] I.S. Wani, et al., Ultrafine-grained AlCoCrFeNi_{2.1} eutectic high-entropy alloy, Mater. Res. Lett. vol. 4 (3) (2016) 174–179, <https://doi.org/10.1080/21663831.2016.1160451>.
- [4] X. Gao, et al., Microstructural origins of high strength and high ductility in an AlCoCrFeNi_{2.1} eutectic high-entropy alloy, Acta Mater. vol. 141 (2017) 59–66, <https://doi.org/10.1016/j.actamat.2017.07.041>.
- [5] J. Ren, et al., Strong yet ductile nanolamellar high-entropy alloys by additive manufacturing, Nature vol. 608 (7921) (2022) 62–68, <https://doi.org/10.1038/s41586-022-04914-8>.
- [6] Q. Sui et al., The microstructure and mechanical properties of the additive manufactured AlCoCrFeNi high entropy alloy, Mater. Sci. Eng. A, vol. 833, no. December 2021, p. 142507, 2022, doi: 10.1016/j.msea.2021.142507.
- [7] Y. Dong, X. Gao, Y. Lu, T. Wang, T. Li, A multi-component AlCrFe₂Ni₂ alloy with excellent mechanical properties, Mater. Lett. vol. 169 (2016) 62–64, <https://doi.org/10.1016/j.matlet.2016.01.096>.
- [8] X. Chen et al., Effects of aluminum on microstructure and compressive properties of Al-Cr-Fe-Ni eutectic multi-component alloys," Mater. Sci. Eng. A, vol. 681, no. November 2016, pp. 25–31, 2017, doi: 10.1016/j.msea.2016.11.019.
- [9] G. Hillel, L. Natovitz, S. Salhov, S. Haroush, M. Pinkas, L. Meshi, Understanding the role of the constituting elements of the alcofcrfeni high entropy alloy through the investigation of quaternary alloys, Metals vol. 10 (10) (2020) 1–11, <https://doi.org/10.3390/met10101275>.
- [10] A. Munitz, S. Salhov, S. Hayun, N. Frage, Heat treatment impacts the microstructure and mechanical properties of AlCoCrFeNi high entropy alloy, J. Alloy. Compd. vol. 683 (2016) 221–230, <https://doi.org/10.1016/j.jallcom.2016.05.034>.
- [11] P. Shi, et al., Enhanced strength-ductility synergy in ultrafine-grained eutectic high-entropy alloys by inheriting microstructural lamellae, Nat. Commun. vol. 10 (1) (2019) 1–8, <https://doi.org/10.1038/s41467-019-10840-2>.
- [12] U. Hecht, S. Gein, O. Stryzhyboroda, E. Eshed, S. Osovski, The BCC-FCC phase transformation pathways and crystal orientation relationships in dual phase materials from Al-(Co)-Cr-Fe-Ni alloys (no. August), Front. Mater. vol. 7 (2020) 1–11, <https://doi.org/10.3389/fmats.2020.00287>.
- [13] O. Stryzhyboroda, V.T. Witusiewicz, S. Gein, D. Röhrens, U. Hecht, "Phase Equilibria in the Al-Co-Cr-Fe-Ni High Entropy Alloy System: Thermodynamic Description and Experimental Study," (no. August), Front. Mater. vol. 7 (2020) 1–13, <https://doi.org/10.3389/fmats.2020.00270>.
- [14] X. Duan, et al., Cooperative effect of Cr and Al elements on passivation enhancement of eutectic high-entropy alloy AlCoCrFeNi_{2.1} with precipitates, J. Mater. Sci. Technol. vol. 136 (2023) 97–108, <https://doi.org/10.1016/j.jmst.2022.07.023>.
- [15] L. Song, et al., Corrosion behavior of the AlCoCrFeNi_{2.1} eutectic high-entropy alloy in chloride-containing sulfuric acid solutions at different temperatures, Materials vol. 15 (14) (2022) 1–16, <https://doi.org/10.3390/ma15144822>.
- [16] H. Wu, et al., Comparative study of mechanical and corrosion behaviors of cost-effective AlCrFeNi high entropy alloys, J. Mater. Eng. Perform. vol. 31 (6) (2022) 4472–4482, <https://doi.org/10.1007/s11665-021-06563-w>.
- [17] E.M. Godlewska, M. Mitoraj-Krolikowska, J. Czerski, M. Jaworska, S. Gein, U. Hecht, Corrosion of Al(Co)CrFeNi high-entropy alloys (no. October), Front. Mater. vol. 7 (2020) 1–12, <https://doi.org/10.3389/fmats.2020.566336>.
- [18] M. Zhang, X. Shi, Z. Li, H. Xu, G. Li, Corrosion behaviors and mechanism of CrFeNi₂ based high-entropy alloys (no. July, p.), Corros. Sci. vol. 207 (2022) 110562, <https://doi.org/10.1016/j.corsci.2022.110562>.
- [19] P. Cui, et al., Corrosion behavior and mechanism of dual phase Fe_{1.125}Ni_{1.06}Cr₁ high entropy alloy, (no. November 2021, p), Corros. Sci. vol. 201 (2022) 110276, <https://doi.org/10.1016/j.corsci.2022.110276>.
- [20] Q. Zhao, Z. Pan, X. Wang, H. Luo, Y. Liu, X. Li, Corrosion and passive behavior of AlxCrFeNi_{3-x} (x = 0.6, 0.8, 1.0) eutectic high entropy alloys in chloride environment (no. September, p), Corros. Sci. vol. 208 (2022) 110666, <https://doi.org/10.1016/j.corsci.2022.110666>.
- [21] Y.F. Kao, T.D. Lee, S.K. Chen, Y.S. Chang, Electrochemical passive properties of Al_xCoCrFeNi (x = 0, 0.25, 0.50, 1.00) alloys in sulfuric acids, Corros. Sci. vol. 52 (3) (2010) 1026–1034, <https://doi.org/10.1016/j.corsci.2009.11.028>.
- [22] C.C. Yen, et al., Corrosion mechanism of annealed equiatomic AlCoCrFeNi tri-phase high-entropy alloy in 0.5 M H₂SO₄ aerated aqueous solution (no. June), Corros. Sci. vol. 157 (2019) 462–471, <https://doi.org/10.1016/j.corsci.2019.06.024>.
- [23] L. Wei, W. Qin, "Corrosion mechanism of eutectic high-entropy alloy induced by micro-galvanic corrosion in sulfuric acid solution," (no. July), Corros. Sci. vol. 206 (2022) 110525, <https://doi.org/10.1016/j.corsci.2022.110525>.
- [24] R.K. Sim, Z. Xu, M.Y. Wu, A. He, D.L. Chen, and D.Y. Li, "Microstructure, mechanical properties, corrosion and wear behavior of high-entropy alloy AlCoCrFeNi_x (x > 0) and medium-entropy alloy (x = 0)," J. Mater. Sci., vol. 57, no. 25, pp. 11949–11968, 2022, doi: 10.1007/s10853-022-07256-y.
- [25] C. Xiang, Z.M. Zhang, H.M. Fu, E.H. Han, H.F. Zhang, J.Q. Wang, Microstructure and corrosion behavior of AlCoCrFeNiSi_{0.1} high-entropy alloy (no. August), Intermetallics vol. 114 (2019), <https://doi.org/10.1016/j.intermet.2019.106599>.
- [26] X.H. Gu, H.J. Yan, Q.H. Zhang, X.Z. Meng, L.K. Wu, F.H. Cao, Microstructure characterization and corrosion behavior of Al_x(CoCrFeNi)_{100-x} (x = 0, 5, 10, 15, 20) high entropy alloys in 0.5 M H₂SO₄ solution, J. Alloy. Compd. vol. 944 (2023) 169247, <https://doi.org/10.1016/j.jallcom.2023.169247>.
- [27] X.H. Gu, X. ran Li, Q. hao Zhang, L.K. Wu, and F.H. Cao, Passive film and surface characterization of Al_x(CoCrFeNi)_{100-x} (x = 0, 5, 10, 15, 20) high entropy alloys," Intermetallics, vol. 162, 107994, Nov. 2023, doi: 10.1016/j.intermet.2023.107994.
- [28] S. Maximovitch, G. Barral, F. Le Cras, and F. Claudet, "Electrochemical incorporation of molybdenum in the passive layer of a 17% Cr ferritic stainless steel," Mater. Sci. Forum, vol. 192–194, no. pt 1, pp. 111–120, 1995, doi: 10.4028/www.scientific.net/msf.192-194.111.
- [29] Z. Wang, E.M. Paschalidou, A. Seyeux, S. Zanna, V. Maurice, P. Marcus, Mechanisms of Cr and Mo enrichments in the passive oxide film on 316L austenitic stainless steel (no. September), Front. Mater. vol. 6 (2019) 1–12, <https://doi.org/10.3389/fmats.2019.00232>.
- [30] K. Hashimoto, K. Asami, A. Kawashima, H. Habazaki, E. Akiyama, The role of corrosion-resistant alloying elements in passivity, Corros. Sci. vol. 49 (1) (2007) 42–52, <https://doi.org/10.1016/j.corsci.2006.05.003>.
- [31] A. Pardo, M.C. Merino, A.E. Coy, F. Viejo, R. Arrabal, E. Matykina, Effect of Mo and Mn additions on the corrosion behaviour of AISI 304 and 316 stainless steels in H₂SO₄, Corros. Sci. vol. 50 (3) (2008) 780–794, <https://doi.org/10.1016/j.corsci.2007.11.004>.
- [32] Y.S. Kim, Influences of alloyed molybdenum and molybdate addition on the corrosion properties and passive film composition of stainless steels, Met. Mater. Int. vol. 4 (2) (1998) 183–191, <https://doi.org/10.1007/BF03026036>.
- [33] H.Y. Ha, T.H. Lee, J.H. Bae, D.W. Chun, Molybdenum effects on pitting corrosion resistance of FeCrMnMoN_C austenitic stainless steels, Metals vol. 8 (8) (2018) 1–13, <https://doi.org/10.3390/met8080653>.
- [34] J. Liu, X. An, J. Zhang, Q. Kong, Q. Li, H. Wang, Microstructure, mechanical and corrosion properties of Co- and Cu-free AlxCrFeNi_{2.5Mo1-x} high entropy alloys,

- no. September 2022, p, *Intermetallics* vol. 153 (2023) 107775, <https://doi.org/10.1016/j.intermet.2022.107775>.
- [35] Q. Hu, C.P. Ye, S.C. Zhang, X.Z. Wang, C.F. Du, H. Wang, Mo content depended competition between Cr₂O₃ enrichment and selective dissolution of CoCrFeNiMox high entropy alloys, *npj Mater. Degrad.* vol. 6 (1) (2022) 1–14, <https://doi.org/10.1038/s41529-022-00313-6>.
- [36] X.L. Shang, Z.J. Wang, Q.F. Wu, J.C. Wang, J.J. Li, J.K. Yu, Effect of Mo addition on corrosion behavior of high-entropy alloys CoCrFeNiMox in aqueous environments, *Acta Metall. Sin. (Engl. Lett.)* vol. 32 (1) (2019) 41–51, <https://doi.org/10.1007/s40195-018-0812-7>.
- [37] C. Dai, T. Zhao, C. Du, Z. Liu, D. Zhang, Effect of molybdenum content on the microstructure and corrosion behavior of FeCoCrNiMox high-entropy alloys, *J. Mater. Sci. Technol.* vol. 46 (2020) 64–73, <https://doi.org/10.1016/j.jmst.2019.10.020>.
- [38] C. Dai, H. Luo, J. Li, C. Du, Z. Liu, J. Yao, X-ray photoelectron spectroscopy and electrochemical investigation of the passive behavior of high-entropy FeCoCrNiMox alloys in sulfuric acid, no. May 2019, p, *Appl. Surf. Sci.* vol. 499 (2020) 143903, <https://doi.org/10.1016/j.apsusc.2019.143903>.
- [39] X. Wang, et al., Enhanced passivity of Cr-Fe-Co-Ni-Mo multi-component single-phase face-centred cubic alloys: design, production and corrosion behaviour (no. January), *Corros. Sci.* vol. 200 (2022), <https://doi.org/10.1016/j.corsci.2022.110233>.
- [40] A.A. Rodriguez, et al., Effect of molybdenum on the corrosion behavior of high-entropy alloys CoCrFeNi2 and CoCrFeNi2Mo0.25 under sodium chloride aqueous conditions, *Adv. Mater. Sci. Eng.* vol. (2018) 1–11, 2018, doi: 10.1155/2018/3016304.
- [41] Z. Niu, Y. Wang, C. Geng, J. Xu, Y. Wang, Microstructural evolution, mechanical and corrosion behaviors of as-annealed CoCrFeNiMox ($x = 0, 0.2, 0.5, 0.8, 1$) high entropy alloys, *J. Alloy. Compd.* vol. 820 (2020) 153273, <https://doi.org/10.1016/j.jallcom.2019.153273>.
- [42] Y.L. Chou, J.W. Yeh, H.C. Shih, The effect of molybdenum on the corrosion behaviour of the high-entropy alloys Co1.5CrFeNi1.5Ti0.5Mox in aqueous environments, *Corros. Sci.* vol. 52 (8) (2010) 2571–2581, <https://doi.org/10.1016/j.corsci.2010.04.004>.
- [43] C.B. Nascimento, U. Donatus, C.T. Ríos, M.C.L. De Oliveira, R.A. Antunes, A review on corrosion of high entropy alloys: exploring the interplay between corrosion properties, alloy composition, passive film stability and materials selection, *Mater. Res.* vol. 25 (2022), <https://doi.org/10.1590/1980-5373-MR-2021-0442>.
- [44] J. Michalska, M. Sozańska, Qualitative and quantitative analysis of σ and χ phases in 2205 duplex stainless steel, no. 4–5 SPEC. ISS. Mater. Charact. vol. 56 (2006) 355–362, <https://doi.org/10.1016/j.matchar.2005.11.003>.
- [45] H.M. Ezuber, A. El-Houd, F. El-Shawesh, Effects of sigma phase precipitation on seawater pitting of duplex stainless steel, no. 1–3, *Desalination* vol. 207 (2007) 268–275, <https://doi.org/10.1016/j.desal.2006.05.021>.
- [46] D. Vogiatzief, A. Evrigen, S. Gein, V.R. Molina, A. Weisheit, M. Pedersen, Laser powder bed fusion and heat treatment of an AlCrFe2Ni2 high entropy alloy (no. July), *Front. Mater.* vol. 7 (2020) 1–12, <https://doi.org/10.3389/fmats.2020.00248>.
- [47] D. Vogiatzief, A. Evrigen, M. Pedersen, U. Hecht, Laser powder bed fusion of an Al-Cr-Fe-Ni high-entropy alloy produced by blending of prealloyed and elemental powder: process parameters, microstructures and mechanical properties, *J. Alloy. Compd.* vol. 918 (2022) 165658, <https://doi.org/10.1016/j.jallcom.2022.165658>.
- [48] V.R. Molina, A. Weisheit, S. Gein, U. Hecht, D. Vogiatzief, Laser metal deposition of ultra-fine duplex AlCrFe2Ni2-based high-entropy alloy (no. August), *Front. Mater.* vol. 7 (2020) 1–10, <https://doi.org/10.3389/fmats.2020.00275>.
- [49] S.K. Rittinghaus, A. Ali, U. Hecht, Intrinsic heat treatment of an additively manufactured medium entropy AlCrFe2Ni2-alloy (no. June), *Met. Mater. Int.* (2022), <https://doi.org/10.1007/s12540-022-01246-0>.
- [50] D. Vogiatzief, et al., Effect of heat treatment on mechanical and corrosion properties of an Al0.8CrFe2Ni2 alloy processed by laser powder bed fusion, *J. Alloy. Compd.* vol. 953 (2023) 169816, <https://doi.org/10.1016/j.jallcom.2023.169816>.
- [51] Q. An, et al., Effects of C and Mo on microstructures and mechanical properties of dual-phase high entropy alloys, no. August 2018, *Intermetallics* vol. 110 (2019), <https://doi.org/10.1016/j.intermet.2019.04.014>.
- [52] Y. Dong, Y. Lu, J. Kong, J. Zhang, T. Li, Microstructure and mechanical properties of multi-component AlCrFeNiMox high-entropy alloys, *J. Alloy. Compd.* vol. 573 (2013) 96–101, <https://doi.org/10.1016/j.jallcom.2013.03.253>.
- [53] S. Gein, V.T. Witusiewicz, U. Hecht, The influence of Mo additions on the microstructure and mechanical properties of AlCrFe2Ni2 medium entropy alloys (no. September), *Front. Mater.* vol. 7 (2020) 1–12, <https://doi.org/10.3389/fmats.2020.00296>.
- [54] C.Y. Hsu, T.S. Sheu, J.W. Yeh, S.K. Chen, Effect of iron content on wear behavior of AlCrCrFeMo0.5Ni high-entropy alloys, *Wear* vol. 268 (5–6) (2010) 653–659, <https://doi.org/10.1016/j.wear.2009.10.013>.
- [55] C. Hsu, C. Juan, W. Wang, T. Sheu, J. Yeh, S. Chen, On the superior hot hardness and softening resistance of AlCoCr_xFeMo0.5Ni high-entropy alloys, no. 10–11, *Mater. Sci. Eng. A* vol. 528 (2011) 3581–3588, <https://doi.org/10.1016/j.msea.2011.01.072>.
- [56] S. Esmailzadeh, M. Aliofkhazraei, H. Sarlak, Interpretation of cyclic potentiodynamic polarization test results for study of corrosion behavior of metals: a review, *Prot. Met. Phys. Chem. Surf.* vol. 54 (5) (2018) 976–989, <https://doi.org/10.1134/S207020511805026X>.
- [57] L. Wang, et al., Study of the surface oxides and corrosion behaviour of an equiautomatic CoCrFeMnNi high entropy alloy by XPS and ToF-SIMS, no. December 2019, p, *Corros. Sci.* vol. 167 (2020) 108507, <https://doi.org/10.1016/j.corsci.2020.108507>.
- [58] A. Wetzel, M. von der Au, P.M. Dietrich, J. Radnik, O. Ozcan, J. Witt, The comparison of the corrosion behavior of the CrCoNi medium entropy alloy and CrMnFeCoNi high entropy alloy (no. July), *Appl. Surf. Sci.* vol. 601 (2022), <https://doi.org/10.1016/j.apsusc.2022.154171>.
- [59] B.R. Strohmeier, An ESCA method for determining the oxide thickness on aluminum alloys, *Surf. Interface Anal.* vol. 15 (1) (1990) 51–56, <https://doi.org/10.1002/sia.740150109>.
- [60] B. Jegdić, D.M. Dražić, J.P. Popić, Corrosion potential of 304 stainless steel in sulfuric acid, *J. Serb. Chem. Soc.* vol. 71 (5) (2006) 543–551, <https://doi.org/10.2298/JSC0605543J>.
- [61] M.C. Biesinger, B.P. Payne, A.P. Grosvenor, L.W.M. Lau, A.R. Gerson, R.S.C. Smart, Resolving surface chemical states in XPS analysis of first row transition metals, oxides and hydroxides: Cr, Mn, Fe, Co and Ni, *Appl. Surf. Sci.* vol. 257 (7) (2011) 2717–2730, <https://doi.org/10.1016/j.apsusc.2010.10.051>.
- [62] A.P. Grosvenor, B.A. Kobe, M.C. Biesinger, N.S. McIntyre, Investigation of multiplet splitting of Fe 2p XPS spectra and bonding in iron compounds, *Surf. Interface Anal.* vol. 36 (12) (2014) 1564–1574, <https://doi.org/10.1002/sia.1984>.
- [63] M.C. Biesinger, L.W.M. Lau, A.R. Gerson, R.S.C. Smart, The role of the Auger parameter in XPS studies of nickel metal, halides and oxides, *Phys. Chem. Chem. Phys.* vol. 14 (7) (2012) 2434–2442, <https://doi.org/10.1039/c2cp22419d>.
- [64] M.C. Biesinger, B.P. Payne, L.W.M. Lau, A. Gerson, R.S.C. Smart, X-ray photoelectron spectroscopic chemical state Quantification of mixed nickel metal, oxide and hydroxide systems, *Surf. Interface Anal.* vol. 41 (4) (2009) 324–332, <https://doi.org/10.1002/sia.3026>.
- [65] J. Baltrusaitis, et al., Generalized molybdenum oxide surface chemical state XPS determination via informed amorphous sample model, *Appl. Surf. Sci.* vol. 326 (2015) 151–161, <https://doi.org/10.1016/j.apsusc.2014.11.077>.
- [66] C.R. Clayton, Y.C. Lu, A bipolar model of the passivity of stainless steel: the role of Mo addition, *J. Electrochem. Soc.* vol. 133 (12) (1986) 2465–2473, <https://doi.org/10.1149/1.2108451>.
- [67] V. Maurice, H. Peng, L.H. Klein, A. Seyeux, S. Zanna, P. Marcus, Effects of molybdenum on the composition and nanoscale morphology of passivated austenitic stainless steel surfaces, *Faraday Discuss.* vol. 180 (2015) 151–170, <https://doi.org/10.1039/c4fd00231h>.
- [68] A. Turnbull, M. Ryan, W. Anthony, S. Zhou, Corrosion and electrochemical behaviour of 316L stainless steel in acetic acid solutions, *Corros. Sci.* vol. 45 (5) (2003) 1051–1072, [https://doi.org/10.1016/S0010-938X\(02\)00149-X](https://doi.org/10.1016/S0010-938X(02)00149-X).
- [69] M. Ben Salah, et al., Passivation behaviour of stainless steel (UNS N-08028) in industrial or simplified phosphoric acid solutions at different temperatures, *Corros. Sci.* vol. 99 (2015) 320–332, <https://doi.org/10.1016/j.corsci.2015.07.025>.
- [70] C.O.A. Olsson, D. Landolt, Passive films on stainless steels - chemistry, structure and growth, no. 9 SPEC. *Electrochim. Acta* vol. 48 (2003) 1093–1104, [https://doi.org/10.1016/S0013-4686\(02\)00841-1](https://doi.org/10.1016/S0013-4686(02)00841-1).
- [71] C.B. Nascimento, U. Donatus, C.T. Ríos, R.A. Antunes, Electronic properties of the passive films formed on CoCrFeNi and CoCrFeNiAl high entropy alloys in sodium chloride solution, *J. Mater. Res. Technol.* vol. 9 (6) (2020) 13879–13892, <https://doi.org/10.1016/j.jmrt.2020.10.002>.
- [72] K.M. Hsu, S.H. Chen, C.S. Lin, Microstructure and corrosion behavior of FeCrNiCoMnx ($x = 1.0, 0.6, 0.3, 0$) high entropy alloys in 0.5 M H₂SO₄ (no. July, p), *Corros. Sci.* vol. 190 (2021) 109694, <https://doi.org/10.1016/j.corsci.2021.109694>.
- [73] M. Ray, V.B. Singh, Effect of sulfuric acid on corrosion and passivation of 316 SS in organic solution, *J. Electrochem. Soc.* vol. 158 (11) (2011) C359, <https://doi.org/10.1149/2.047111j>.
- [74] C. Boissy, B. Ter-Ovanessian, N. Mary, B. Normand, Correlation between predictive and descriptive models to characterize the passive film - study of pure chromium by electrochemical impedance spectroscopy, *Electrochim. Acta* vol. 174 (2015) 430–437, <https://doi.org/10.1016/j.electacta.2015.05.179>.
- [75] A. Raza, S. Abdullaahad, B. Kang, H.J. Ryu, S.H. Hong, Corrosion resistance of weight reduced AlCrFeMoV high entropy alloys (no. April), *Appl. Surf. Sci.* vol. 485 (2019) 368–374, <https://doi.org/10.1016/j.apsusc.2019.03.173>.
- [76] B. Hirschorn, M.E. Orazem, B. Tribollet, V. Vivier, I. Frateur, M. Musiani, Determination of effective capacitance and film thickness from constant-phase-element parameters, *Electrochim. Acta* vol. 55 (21) (2010) 6218–6227, <https://doi.org/10.1016/j.electacta.2009.10.065>.
- [77] J. Wu, S.D. Zhang, W.H. Sun, Y. Gao, J.Q. Wang, Enhanced corrosion resistance in Fe-based amorphous coatings through eliminating Cr-depleted zones (no. March), *Corros. Sci.* vol. 136 (2018) 161–173, <https://doi.org/10.1016/j.corsci.2018.03.005>.
- [78] G.T. Burstein, P.I. Marshall, Growth of passivating films on scratched 304L stainless steel in alkaline solution, *Corros. Sci.* vol. 23 (2) (1983) 125–137, [https://doi.org/10.1016/0010-938X\(83\)90111-7](https://doi.org/10.1016/0010-938X(83)90111-7).
- [79] A. Tanjir, R. Feng, Z. Lyu, R. Sakidja, P.K. Liaw, H. Hermawan, Passivity of AlCrFeMnTi and AlCrFeCoNi high-entropy alloys in Hanks' solution, no. August 2022, *Corros. Sci.* vol. 210 (2023), <https://doi.org/10.1016/j.corsci.2022.110828>.
- [80] E.A. Cho, C.K. Kim, J.S. Kim, H.S. Kwon, Quantitative analysis of repassivation kinetics of ferritic stainless steels based on the high field ion conduction model, *Electrochim. Acta* vol. 45 (12) (2000) 1933–1942, [https://doi.org/10.1016/S0013-4686\(99\)00415-6](https://doi.org/10.1016/S0013-4686(99)00415-6).
- [81] G.T. Burstein, A.J. Davenport, The current-time relationship during anodic oxide film growth under high electric field, *J. Electrochem. Soc.* vol. 136 (4) (1989) 936–941, <https://doi.org/10.1149/1.2096890>.

- [82] E. Ura-Binczyk, et al., Passivation of Al-Cr-Fe and Al-Cu-Fe-Cr complex metallic alloys in 1M H₂SO₄ and 1M NaOH solutions, Corros. Sci. vol. 53 (5) (2011) 1825–1837, <https://doi.org/10.1016/j.corsci.2011.01.061>.
- [83] Y. Shi, L. Collins, N. Balke, P.K. Liaw, B. Yang, “In-situ electrochemical-AFM study of localized corrosion of AlxCrFeNi high-entropy alloys in chloride solution,”, Appl. Surf. Sci. vol. 439 (2018) 533–544, <https://doi.org/10.1016/j.apsusc.2018.01.047>.
- [84] E. Akiyama, A. Kawashima, K. Asami, K. Hashimoto, A study of the structure of a passive film using angle-resolved x-ray photo-electron spectroscopy, Corros. Sci. vol. 38 (7) (1996) 1127–1140, [https://doi.org/10.1016/0010-938X\(96\)81813-0](https://doi.org/10.1016/0010-938X(96)81813-0).
- [85] B. Hirschorn, M.E. Orazem, B. Tribollet, V. Vivier, I. Frateur, M. Musiani, Constant-phase-element behavior caused by resistivity distributions in films, J. Electrochem. Soc. vol. 157 (12) (2010) C458, <https://doi.org/10.1149/1.3499565>.
- [86] N. Wurzler, O. Sobol, K. Altmann, J. Radnik, O. Ozcan, Preconditioning of AISI 304 stainless steel surfaces in the presence of flavins—Part I: Effect on surface chemistry and corrosion behavior, Mater. Corros. vol. 72 (6) (2021) 974–982, <https://doi.org/10.1002/maco.202012191>.
- [87] J. Robertson, High dielectric constant oxides, Eur. Phys. J. Appl. Phys. vol. 28 (3) (2004) 265–291, <https://doi.org/10.1051/epjap.2004206>.
- [88] H. Luo, S. Zou, Y.H. Chen, Z. Li, C. Du, X. Li, Influence of carbon on the corrosion behaviour of interstitial equiatomic CoCrFeMnNi high-entropy alloys in a chlorinated concrete solution, no. June 2019, p, Corros. Sci. vol. 163 (2020) 108287, <https://doi.org/10.1016/j.corsci.2019.108287>.
- [89] N.E. Hakiki, M. Da Cunha Belo, A.M.P. Simões, M.G.S. Ferreira, Semiconducting properties of passive films formed on stainless steels: influence of the alloying elements, J. Electrochem. Soc. vol. 145 (11) (1998) 3821–3829, <https://doi.org/10.1149/1.1838880>.
- [90] M.E. Orazem, N. Pébère, B. Tribollet, Enhanced graphical representation of electrochemical impedance data, J. Electrochem. Soc. vol. 153 (4) (2006) B129, <https://doi.org/10.1149/1.2168377>.
- [91] L. Zhang, et al., The effect of potential on surface characteristic and corrosion resistance of anodic oxide film formed on commercial pure titanium at the potentiodynamic-aging mode, Materials vol. 12 (3) (2019), <https://doi.org/10.3390/ma12030370>.
- [92] Y. Shi, B. Yang, X. Xie, J. Brechtl, K.A. Dahmen, P.K. Liaw, Corrosion of AlxCrFeNi high-entropy alloys: Al-content and potential scan-rate dependent pitting behavior, Corros. Sci. vol. 119 (2017) 33–45, <https://doi.org/10.1016/j.corsci.2017.02.019>.
- [93] P. Keller, H.H. Strehblow, XPS investigations of electrochemically formed passive layers on Fe/Cr-alloys in 0.5 M H₂SO₄, Corros. Sci. vol. 46 (8) (2004) 1939–1952, <https://doi.org/10.1016/j.corsci.2004.01.007>.
- [94] C. jie Wang, Q. jun Chen, and H. xiao Xia, “Optimization of Cr/Mo molar ratio in FeCoCrMoCBY alloys for high corrosion resistance,” Trans. Nonferrous Met. Soc. China (English Ed. , vol. 27, no. 12, pp. 2663–2672, Dec. 2017, doi: [10.1016/S1003-6326\(17\)60295-4](https://doi.org/10.1016/S1003-6326(17)60295-4).